J. Fluid Mech. (2011), *vol.* 666, *pp.* 5–35.
doi:10.1017/S0022112010003733

Decay laws, anisotropy and cyclone–anticyclone asymmetry in decaying rotating turbulence

F. MOISY[1]†, C. MORIZE[1], M. RABAUD[1] AND J. SOMMERIA[2]

[1]Laboratoire FAST, Université Paris-Sud 11, Université Pierre et Marie Curie, CNRS, Bâtiment 502, F-91405 Orsay Cedex, France

[2]Coriolis/LEGI, 21 avenue des Martyrs, F-38000 Grenoble, France

(Received 4 September 2009; revised 9 July 2010; accepted 10 July 2010; first published online 12 October 2010)

The effect of a background rotation on the decay of grid-generated turbulence is investigated from experiments using the large-scale 'Coriolis' rotating platform. A first transition occurs at 0.4 tank rotation (instantaneous Rossby number $Ro \simeq 0.25$), characterized by a $t^{-6/5} \to t^{-3/5}$ transition of the energy-decay law. After this transition, anisotropy develops in the form of vertical layers, where the initial vertical velocity fluctuations remain trapped. The vertical vorticity field develops a cyclone–anticyclone asymmetry, reproducing the growth law of the vorticity skewness, $S_\omega(t) \simeq (\Omega t)^{0.7}$, reported by Morize, Moisy & Rabaud (*Phys. Fluids*, vol. 17 (9), 2005, 095105). A second transition is observed at larger time, characterized by a return to vorticity symmetry. In this regime, the layers of nearly constant vertical velocity become thinner as they are advected and stretched by the large-scale horizontal flow, and eventually become unstable. The present results indicate that the shear instability of the vertical layers contributes significantly to the re-symmetrization of the vertical vorticity at large time, by re-injecting vorticity fluctuations of random sign at small scales. These results emphasize the importance of the nature of the initial conditions in the decay of rotating turbulence.

Key words: rotating flows, rotating turbulence, wave–turbulence interactions

1. Introduction

Turbulence subjected to solid-body rotation is a problem of first importance for engineering, geophysical and astrophysical flows. Its dynamics is dictated by a competition between linear and nonlinear effects. Linear effects, driven by the Coriolis force, include anisotropic propagation of energy by inertial waves (IWs), preferentially along the rotation axis (hereafter referred to as 'vertical' axis by convention), on the time scale of the system rotation, Ω^{-1} (Greenspan 1968). Nonlinear interactions, on the other hand, are responsible for energy transfers towards 'horizontal' modes (Cambon & Jacquin 1989; Waleffe 1993). For infinite rotation rate, i.e. for vanishing Rossby number, these IWs reduce to Taylor–Proudman columns, corresponding to a two-dimensional flow (2D) invariant along the rotation axis. Importantly, this 2D flow is not two-component (2C) in general, because the third (vertical) velocity component, insensitive to the Coriolis force, behaves as a passive scalar field

† Email address for correspondence: moisy@fast.u-psud.fr

transported by the horizontal flow. This 'passive' vertical velocity, originating from the initial conditions in the case of decaying turbulence, may, however, become 'active' through shear instabilities at small scale. This mechanism may have considerable importance in the nature of the decay and the partial two-dimensionalization of an initially three-dimensional (3D) turbulence subjected to background rotation.

This paper reports an experimental study of the influence of the background rotation on the decay of an initially isotropic turbulence. Turbulence is generated by translating a grid in a channel mounted on the large-scale 'Coriolis' rotating platform. The aim of this paper is first to characterize, in detail, the decay law of the energy, in a situation of weak lateral confinement. This situation contrasts with the previous experiments by Morize, Moisy & Rabaud (2005) and Morize & Moisy (2006), performed in a rotating tank with an aspect ratio of order one, showing significant confinement effects. Second, the anisotropy growth is investigated, with the aim to characterize the influence at large time of the initial vertical fluctuations on the vertical vorticity statistics.

For turbulence which is subjected to moderate rotation (Rossby number $Ro \simeq O(1)$), the linear and nonlinear time scales are of the same order, resulting in a complex interplay between linear-energy propagation by IWs and anisotropic energy transfers by nonlinear interactions. This complexity is unavoidable in decaying rotating turbulence starting from large initial Rossby number, in which the instantaneous Rossby number decays and crosses $O(1)$ at some transition time. At this time, in the so-called 'intermediate-Rossby-number range' (Bourouiba & Bartello 2007), the effects of the rotation, namely the anisotropy growth and the cyclone–anticyclone symmetry breaking, become significant, and accumulate as time proceeds. Accordingly, the statistical properties of the rotating turbulence at large time are the result of the turbulence history integrated from the initial state and may therefore depend on the details of the initial state. Generic properties should, however, be expected if the initial state is 3D isotropic turbulence with $Ro \gg 1$, which is the situation examined in this paper.

Because of the fast growth of the vertical correlation due to IW propagation (Jacquin *et al.* 1990; Squires *et al.* 1994), confinement along the vertical axis plays a significant role in the dynamics of rotating turbulence, therefore comparisons with homogeneous turbulence in idealized unbounded systems should be made carefully. One consequence of the vertical confinement is a preferential alignment of the axis of the vortices normal to the walls, therefore reinforcing the 2D nature of the large scales, as observed by Hopfinger, Browand & Gagne (1982) and Godeferd & Lollini (1999). Second, confinement selects a set of discrete resonant inertial modes (Dalziel 1992; Maas 2003; Bewley *et al.* 2007), which may couple to the small-scale turbulence. Third, an extra mechanism of dissipation of the IWs takes place in the boundary layers, acting on the Ekman time scale $h(\nu\Omega)^{-1/2}$, where h is the confinement scale along the rotation axis, which may dominate the energy decay at large time (Phillips 1963; Ibbetson & Tritton 1975; Morize & Moisy 2006).

The most remarkable feature of rotating turbulence is the spontaneous emergence of long-lived columnar vortices aligned with the rotation axis (Hopfinger *et al.* 1982; Smith & Waleffe 1999; Longhetto *et al.* 2002). Nonlinear mechanisms (Cambon & Scott 1999; Cambon 2001) and linear mechanisms (Davidson, Staplehurst & Dalziel 2006; Staplehurst, Davidson & Dalziel 2008) have been proposed to explain the formation of these columnar structures, and the interplay between the two is still a matter of debate. The recent numerical simulations of Yoshimatsu, Midorikawa &

Kaneda (2010) suggest that both effects should be actually considered to account for the formation of these vertical structures.

A striking property of these vortices for intermediate Rossby numbers is the symmetry breaking between cyclones and anticyclones, observed both in forced (Hopfinger *et al.* 1982; Smith & Lee 2005) and decaying (Bartello, Métais & Lesieur 1994; Smith & Waleffe 1999) turbulence. This symmetry breaking has received considerable interest in recent years. It has been quantified in terms of the vorticity skewness, $S_\omega = \langle \omega_z^3 \rangle / \langle \omega_z^2 \rangle^{3/2}$ (where ω_z is the vorticity component along the rotation axis), which is found to be positive for $Ro \simeq 1$ (Bartello *et al.* 1994; Morize *et al.* 2005; Bourouiba & Bartello 2007; van Bokhoven *et al.* 2008; Staplehurst *et al.* 2008; Yoshimatsu *et al.* 2010). In decaying rotating turbulence, starting from initial conditions such that $Ro \gg 1$, a power-law growth has been observed in the form $S_\omega \simeq (\Omega t)^{0.6 \pm 0.1}$ by Morize *et al.* (2005), suggesting a build-up of vorticity skewness acting on the linear time scale Ω^{-1}.

Several explanations have been proposed for the cyclone–anticyclone asymmetry growth, although none provides a complete description of the experimental data. First, in a rotating frame, for a given vertical strain, $\partial u_z / \partial z$, the vortex stretching of the axial vorticity, $(2\Omega + \omega_z)\partial u_z / \partial z$, is larger for cyclonic than for anticyclonic vorticity. Gence & Frick (2001) have shown that, for isotropic turbulence suddenly subjected to a background rotation, S_ω grows linearly at short time, i.e. for $t \ll \Omega^{-1}$. At larger time, the growth is expected to be slower, because the strain $\partial u_z / \partial z$ is reduced by the rotation. Second, anticyclonic vortices are more prone to centrifugal instabilities. This effect can be readily shown for idealized axisymmetric vortices, for which the generalized Rayleigh criterion in a rotating frame (Kloosterziel & van Heijst 1991) is more likely to become negative for anticyclonic vorticity. Sreenivasan & Davidson (2008) have actually shown, using a model of axisymmetric vortex patches, that cyclonic vortices first develop columnar structures, while anticyclonic vortices become centrifugally unstable.

Interestingly, a return to vorticity symmetry has been reported at large times (smaller Ro values) by Morize *et al.* (2005, 2006). This decrease may originate both from internal (2D) diffusion or Ekman-pumping-induced diffusion of the vortices. On the contrary, vortex merging would lead to an increase in S_ω, similarly to what is observed for the vorticity flatness in 2D turbulence (McWillams 1984; Carnevale *et al.* 1991). The decrease in S_ω was first attributed to confinement effects, more specifically the nonlinear Ekman pumping on the rigid walls. However, this was questioned by the results of van Bokhoven *et al.* (2008), in which a decrease of S_ω is also observed at large times, but in a numerical simulation with periodic boundary conditions, and hence, without Ekman pumping. According to these authors, the decrease in S_ω is an effect of the phase mixing of IWs, which damps all triple correlations of turbulent fields in the limit of low Rossby numbers.

The non-monotonic time evolution of the vorticity skewness is confirmed by the present experiments, although the boundary conditions significantly differ from those of Morize *et al.* (2005). The present results suggest an additional contribution for this decrease at large times: as time proceeds, the vertical velocity, initiated by the 3D initial conditions, forms vertically coherent layers transported by the large-scale quasi-2D flow. The horizontal straining of these layers by the large-scale structures produces smaller scales, in a process similar to the enstrophy cascade in 2D turbulence. This mechanism reinforces the horizontal gradient of the vertical velocity, making these layers prone to inertial instabilities, producing small-scale horizontal vorticity. This horizontal vorticity produces in turn random vertical vorticity, resulting in a

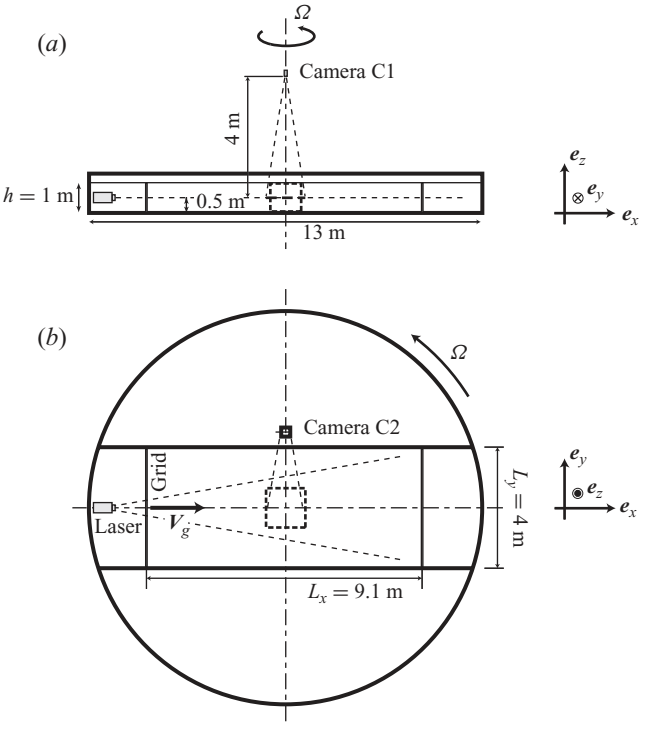

FIGURE 1. Side view (*a*) and top view (*b*) of the experimental set-up. The grid is translated from left to right along $\boldsymbol{e}_x$. The angular velocity is $\boldsymbol{\Omega} = \Omega \boldsymbol{e}_z$, with $\Omega > 0$ (anticlockwise rotation). The PIV camera is located either at C1 or C2, for measurements in the horizontal and vertical planes, respectively. The dashed squares show the corresponding imaged areas.

reduction of S_ω at large times. This re-injection of symmetric vorticity fluctuations at small scale is thought to be a generic mechanism in decaying rotating turbulence, provided the initial state contains a significant amount of vertical velocity, which is the case for an initial 3D isotropic turbulence.

This paper is organized as follows. Section 2 describes the experimental set-up, the particle-image-velocimetry (PIV) measurements and discusses the separation between the mean flow and the turbulence. The influence of the background rotation on the energy decay and the time evolution of the non-dimensional numbers are presented in § 3. The anisotropy growth and the formation of the vertical layers are characterized in § 4. The structure and dynamics of the vertical vorticity field is described in § 5, with emphasis on the cyclone–anticyclone asymmetry growth and the influence of the shear instability of the vertical layers. Finally, § 6 summarizes the different regimes observed during the decay.

2. Experimental set-up and procedure

2.1. *Experimental apparatus*

The experimental set-up, shown in figure 1, consists of a $13\,\mathrm{m} \times 4\,\mathrm{m}$ water channel, filled to a depth of $h = 1\,\mathrm{m}$, mounted on the Coriolis rotating platform. Details about the rotating platform may be found in Praud, Fincham & Sommeria (2005) and Praud, Sommeria & Fincham (2006), and only the features specific to the present

Rotation period T (s)	∞	120	60	30
Symbol	★	○	□	△
Angular velocity Ω (rad s^{-1})	0	0.052	0.105	0.209
Grid Rossby number Ro_g	∞	20.4	10.2	5.1
Ekman layer thickness δ_E (mm)	∞	4.4	3.1	2.2
Ekman time scale t_E (s)	∞	4370	3090	2185

TABLE 1. Flow parameters. The symbols are used in the following figures.

experiments are described here. One set of experiments without rotation, and three sets with rotation periods of $T = 30$, 60 and 120 s, have been carried out (see table 1). The angular velocity $\Omega = 2\pi/T$ is constant within a precision of $\Delta\Omega/\Omega < 10^{-4}$. The parabolic elevation of the surface height induced by the rotation along the channel length is 0.3 cm (respectively, 4.5 cm) for the lowest (respectively, highest) rotation rate.

Turbulence is generated by horizontally translating a vertical grid, of width equal to the channel width, at a constant velocity $V_g = 30$ cm s^{-1} over a distance of $L_x = 9.1$ m along the channel (see supplementary movie 1 available at journals.cambridge.org/flm). The streamwise, spanwise and vertical axes are denoted x, y and z, respectively, with $\boldsymbol{e}_x$, $\boldsymbol{e}_y$ and $\boldsymbol{e}_z$ being the corresponding unit vectors. The grid is made of square bars of width $b = 30$ mm, with a mesh size of $M = 140$ mm and a solidity (ratio of closed to mesh area) $\sigma = 1 - (1 - b/M)^2 = 0.38$. The mesh is significantly smaller than the grid cross-section, ensuring weak vertical confinement effects at small time ($h/M = 7$), and negligible lateral confinement effects even at large time ($L_y/M = 28$). The grid is hung from a carriage moving above the free surface. The velocity of the grid increases linearly from 0 to V_g, remains constant in the central part, and decreases linearly back to zero at the end of the channel. The time at which the grid crosses the centre of the channel, where the measurements are performed, defines the origin $t = 0$. Because of the evaporation, a temperature difference may be present between the ambient air and the water, resulting in residual convection cells of maximum velocity of order 1 mm s^{-1} in the absence of forcing and rotation. However, the mixing induced by the grid translation homogenizes the fluid temperature and breaks these residual convective motions, therefore thermal effects could be safely neglected during most of the decay.

The initial conditions of an experiment are characterized by the grid Reynolds and Rossby numbers based on the grid velocity and grid mesh,

$$Re_g = \frac{V_g M}{\nu}, \quad Ro_g = \frac{V_g}{2\Omega M}, \tag{2.1}$$

where ν is the water kinematic viscosity. The grid Reynolds number is constant for all the experiments, $Re_g = 4.20 \times 10^4$, while the grid Rossby number lies in the range 5.1–20.4 (table 1). The Rossby number based on the bar width ranges between 24 and 96, so the turbulent energy production in the near wake of the grid is expected to be weakly affected by the rotation (Khaledi, Barri & Andersson 2009).

2.2. *Particle image velocimetry*

A high-resolution PIV system, based on a 14 bits 2048×2048 pixels camera (PCO.2000), was used in these experiments. Water was seeded by Chemigum P83 particles, 250 μm in diameter, carefully selected to match the water density to better than 10^{-3}. The corresponding settling velocity, of 0.03 mm s^{-1}, is much smaller than

the typical fluid velocity. The flow was illuminated by a laser sheet of thickness 1 cm, generated by a 6 W Argon laser beam and an oscillating mirror. Two fields of view have been used as follows.

(*a*) A centred square area of $1.3\,\mathrm{m} \times 1.3\,\mathrm{m}$ in the horizontal plane $(\boldsymbol{e}_x, \boldsymbol{e}_y)$ at mid-height ($z = 0.5\,\mathrm{m}$). The camera is located 4 m above the horizontal laser sheet (C1 in figure 1), and the area is imaged through the free surface.

(*b*) A $1.1\,\mathrm{m} \times 1\,\mathrm{m}$ area in the vertical plane $(\boldsymbol{e}_x, \boldsymbol{e}_z)$ in the middle of the channel. The plane is imaged through a window in the lateral wall (C2 in figure 1), so that the measurements are not affected by free surface disturbances.

Spatial calibration was achieved by imaging a reference plate at the location of the laser sheet. For the horizontal measurements, the surface elevation of the parabolic surface is less than 2 mm on the imaged area, so the optical distortion could be safely neglected.

Up to six decay experiments of 1 h (7700 grid time scales M/V_g) have been carried out for each rotation rate and, for each decay, 400 image pairs are recorded. Since the characteristic velocity decreases in time, the delay between the two successive images of a pair is made to gradually increase during the acquisition sequence, from 125 ms to 2 s, so that the typical particles displacement remains approximately constant throughout the decay. The time delay between image pairs is also gradually increased during the decay, from 2 to 20 s. The results are ensemble averaged over $N_r = 6$ realizations in the horizontal plane and $N_r = 4$ in the vertical plane. Although this is enough to achieve statistical convergence at small times, when the correlation length is significantly smaller than the imaged area, the convergence becomes questionable at large times, when the imaged area contains on average one large-scale structure or less.

The PIV computations have been performed using the software Davis (LaVision), and the statistical analysis of the velocity fields using the PIVMat toolbox under Matlab. Interrogation windows of size 32×32 pixels, with an overlap of 16 pixels, were used. For this window size, the corresponding particle displacement resolution is better than 0.1 pixel (Raffel *et al.* 2007), yielding a velocity signal-to-noise ratio of 50. The final velocity fields are defined on a 128×128 grid, with a spatial resolution $\Delta x = 10\,\mathrm{mm}$.

Due to this moderate spatial resolution, the velocity field inside the Ekman boundary layer, of thickness $\delta_E = (\nu/\Omega)^{1/2} \simeq 2.2$–$4.4\,\mathrm{mm}$ (see table 1), cannot be resolved. Assuming isotropy in the bulk of the flow, which is valid only in the non-rotating case or at small time, the smallest turbulent scale can be estimated by the Kolmogorov scale $\eta = (\nu^3/\epsilon)^{1/4}$, where the dissipation rate ϵ can be computed from the energy decay, $\epsilon \simeq -(3/2)\partial(u_x')^2/\partial t$ (energy decays are detailed in § 3). The scale η is of order of $0.4\,\mathrm{mm} \simeq \Delta x/25$ at $t \simeq 20M/V_g$, for all rotation rates, so that the smallest scales are not resolved at the beginning of the decay. Accordingly, the measured velocity gradients at scale Δx underestimate the actual ones (Lavoie *et al.* 2007). Velocity gradients can be considered as well resolved when $\Delta x < 3\eta$ (see e.g. Jimenez 1994), which is satisfied for $t > 350M/V_g$ only. At the end of the decay, η is of the order of 8 mm for $\Omega = 0$, in which case the gradients can be accurately computed from the PIV measurements.

Finally, we note that when the flow is imaged from above, an additional source of noise is the refraction through the disturbed free surface, originating either from the wake of the grid or from residual vibrations of the rotating platform. These perturbations generate an additional apparent particle displacement, $\delta\boldsymbol{x}_{FS} = (1 - 1/n_w)\,(h/2)\,\boldsymbol{\nabla} h$, where n_w is the water refraction index, $\boldsymbol{\nabla} h$ is the surface gradient

and $h/2$ is the path length of the refracted light rays (see, e.g. Moisy, Rabaud & Salsac 2009), and hence a velocity contamination of order $|\delta \boldsymbol{x}_{FS}|/\delta t$, with δt the inter-frame time. This velocity contamination has been estimated by imaging a set of fixed particles stuck on a rigid plate and imaged under the same experimental conditions. It was found that the measurements were significantly altered by this contamination during the first 10 s ($\simeq 20M/V_g$) after the grid translation, but were reliable at larger time.

2.3. *Flow visualizations*

First insight into the influence of the background rotation on the turbulence decay may be obtained by comparing the horizontal and vertical vorticity fields shown in figure 2, in the non-rotating case (*a*,*c*) and in an experiment rotating at $\Omega = 0.10\,\mathrm{rad\,s^{-1}}$ (*b*,*d*). These snapshots are obtained 360 s after the grid translation ($770M/V_g$). At this time, the turbulent Reynolds number is 400 and 700 for the non-rotating and rotating cases, respectively, and the macro-Rossby number for the rotating case is 0.06 (these numbers are defined in § 3.4).

While the vorticity fields ω_z and ω_y for the non-rotating cases are similar in the two measurement planes, as expected for approximately isotropic turbulence, they strongly differ in the rotating case. Supplementary movies 2 and 3 of ω_z and ω_y clearly show the two essential features of the turbulence decay in the rotating frame, namely the anisotropy growth in the vertical plane and the cyclone–anticyclone asymmetry in the horizontal plane.

The vertical vorticity, ω_z, shows strong large-scale vortices, mostly cyclonic (in red), surrounded by shear layers. In the vertical plane, the spanwise vorticity, ω_y, shows vertically elongated structures of alternating sign, originating from layers of ascending and descending fluid. The dominant contribution of ω_y comes from the vertical shear, $\partial u_z/\partial x$, except near the top and bottom boundary layers where the horizontal shear $\partial u_x/\partial z$ is dominant.

2.4. *Large-scale flows and Reynolds decomposition*

Translating a grid in a closed volume is ideally designed to produce homogeneous turbulence with zero mean flow. However, reproducible flow features are found over successive realizations (Dalziel 1992), therefore a careful separation between the ensemble average and the turbulent component is necessary. From the time series of the spatially averaged velocity components shown in figure 3, three large-scale flows can be identified:

(i) *Large-scale circulation* (LSC): The grid translation generates a slight mean flow along $x > 0$ in the centre of the channel, of initial amplitude $\simeq 2 \times 10^{-2} V_g$, which recirculates along the lateral walls (out of the measurement area). Moreover, because of the boundary condition asymmetry between the solid boundary at $z = 0$ and the free surface at $z = h$, this streamwise flow has a significant residual shear $\partial \langle U_x \rangle / \partial z > 0$, of initial amplitude $\simeq 0.03 V_g/h \simeq 10^{-2}\,\mathrm{s^{-1}}$.

(ii) *Gravity wave* (GW): As the grid is translated along the channel, it pushes a significant amount of water near the endwall, which initiates a fast longitudinal GW (sloshing mode). Its wavelength, λ, is twice the channel length, and its period, T_{GW}, is 7.3 s.

(iii) *Inertial wave* (IW): When rotation is present, the mean horizontal shear induced by the grid excites an IW, with a period which is half of the rotation period of the tank, $T_{IW} = T/2$. This IW essentially consists of the oscillating shearing motion of two horizontal layers of thickness $h/2$, compatible with a mode of vertical wavevector (Dalziel 1992; Maas 2003). In the horizontal plane, the signature of this IW is a

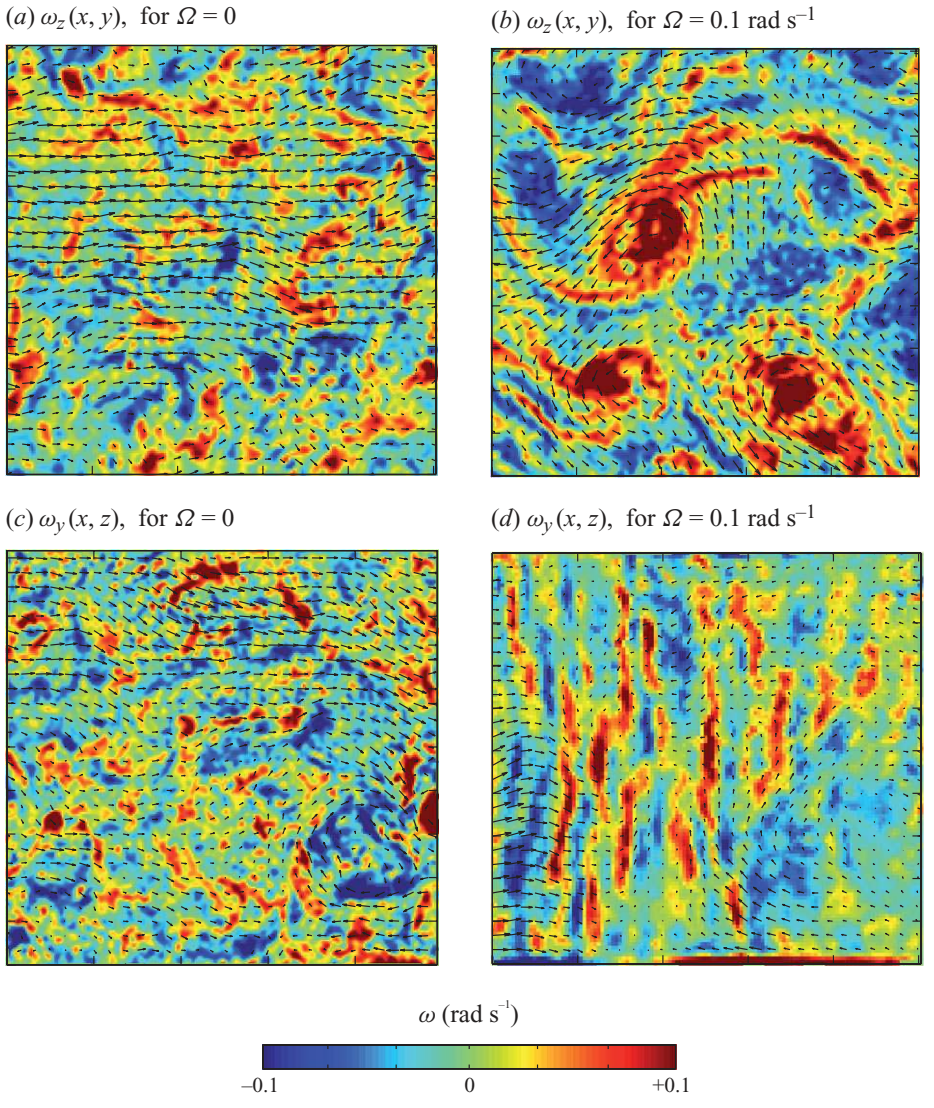

FIGURE 2. Horizontal and vertical snapshots of the velocity fields taken at $t = 360\,\mathrm{s} \simeq 770M/V_g$ after the grid translation, without rotation (a,c) and with rotation at $\Omega = 0.10\,\mathrm{rad\,s^{-1}}$ (b, d). For the rotating cases, this time corresponds to six tank rotations. The imaged area is $1\,\mathrm{m} \times 1\,\mathrm{m}$. The colour shows the vorticity normal to the plane, $\omega_z(x, y)$ and $\omega_y(x, z)$, ranging from -0.1 to $0.1\,\mathrm{rad\,s^{-1}}$. Note the presence of a mean flow in the direction of the grid motion (along $\boldsymbol{e}_x$), with a marked mean shear $\partial\langle U_x\rangle/\partial z$, which is of constant sign for $\Omega = 0$ (c), but oscillating for $\Omega \neq 0$ (d).

uniform anticyclonic oscillation, visible by the phase shift of $\pi/2$ between the mean velocity components $\langle U_x\rangle$ and $\langle U_y\rangle$. Its amplitude is of the order of $U_{IW} \simeq 10^{-2}V_g$ (respectively, $5 \times 10^{-4}V_g$) at the beginning (respectively, end) of the decay.

In the non-rotating case, the mean residual shear persists over large times. Although very weak, it becomes unstable and eventually acts as a source of turbulence. On the other hand, when rotation is present, the oscillation of this large-scale shear is found to have a stabilizing effect. This stabilization is probably due to the fact that

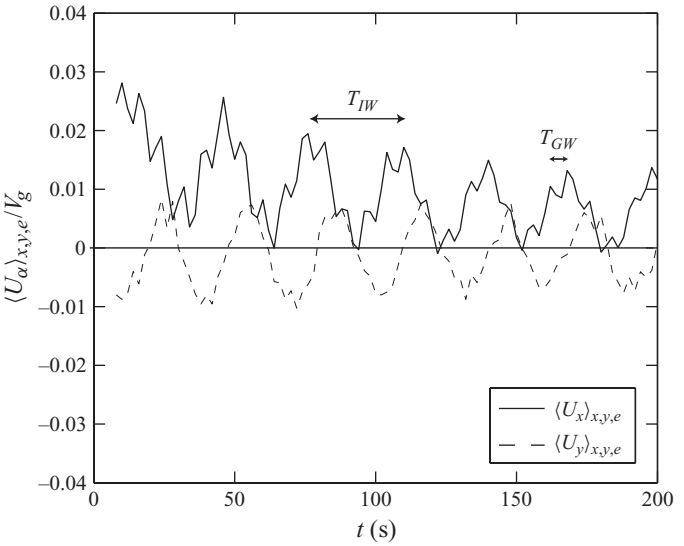

FIGURE 3. Time evolution of the ensemble and spatially averaged streamwise (—) and spanwise (- -) velocity components, for $\Omega = 0.1\,\mathrm{rad\,s^{-1}}$ (rotation period $T = 60\,\mathrm{s}$). The fast oscillation, of period $T_{GW} \simeq 7.3\,\mathrm{s}$, is a longitudinal GW and the slow oscillation, of period $T_{IW} = T/2 = 30\,\mathrm{s}$, is an anticyclonic IW.

the growth time for the shear instability, of the order of $(\partial\langle U_x\rangle/\partial z)^{-1}$, is typically 100 times larger than the oscillation period, π/Ω. As a consequence, at each half period of oscillation, the growth of the shear instability is inhibited (Poulin, Flierl & Pedlosky 2003), resulting in a reduction of the turbulence production.

The measured velocity field $\boldsymbol{U}$ can be written as the sum of the three large-scale flows U_{LSC}, U_{GW} and U_{IW} described above and the turbulent field of interest $\boldsymbol{u}$. Keeping only the dominant spatial dependences of these contributions, one has

$$\boldsymbol{U}^{(n)}(x, y, z, t) \simeq U_{LSC}(z, t)\boldsymbol{e}_x + U_{GW}(t)\cos\left(\frac{2\pi t}{T_{GW}}\right)\boldsymbol{e}_x + U_{IW}(z, t)\left[\cos\left(\frac{2\pi t}{T_{IW}}\right)\boldsymbol{e}_x + \sin\left(\frac{2\pi t}{T_{IW}}\right)\boldsymbol{e}_y\right] + \boldsymbol{u}^{(n)}(x, y, z, t), \quad (2.2)$$

where n is the realization number (the phase origin of the GW and IW flows are not written for simplicity). Since the three large-scale flows are essentially uniform translations, they can be readily subtracted from the measured velocity fields, providing that the turbulent scale is significantly smaller than the field of view. For the measurements in the horizontal plane, one has

$$u_\alpha^{(n)}(x, y, t) = U_\alpha^{(n)}(x, y, t) - \langle U_\alpha^{(n)}(x, y, t)\rangle_{x,y,e}, \quad (2.3)$$

with $\alpha = x, y$. The subscripts indicate the type of average: $\langle\cdot\rangle_{x,y}$ for the spatial average over the x- and y-directions and $\langle\cdot\rangle_e$ for the ensemble average over the independent realizations. Similarly, for the measurements in the vertical plane, the average $\langle\cdot\rangle_{x,z,e}$ is computed. In order to reduce the statistical noise due to the limited number of realizations, a temporal smoothing is also performed. The window size of the temporal smoothing is chosen equal to 5 % of the elapsed time, t, corresponding to a number

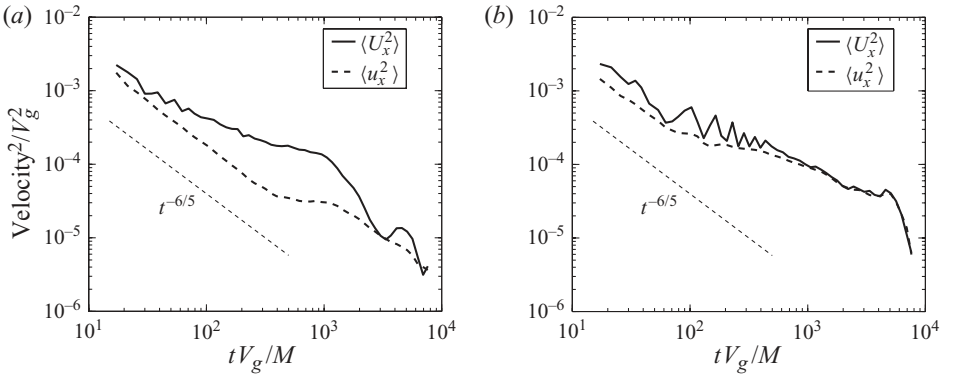

FIGURE 4. Total and turbulent kinetic energy (streamwise variance). (*a*) $\Omega = 0$, (*b*) $\Omega = 0.10\,\mathrm{rad\,s^{-1}}$ ($T = 60\,\mathrm{s}$). The oscillations in the rotating case correspond to IW flow, of period $T_{IW} = T/2 = 30\,\mathrm{s}$.

of consecutive velocity fields of $N_t = 1$ at the beginning (i.e. no average) up to $N_t = 20$ at the end of the decay.

The statistics in the following combine the spatial average over the 128^2 PIV grid points, the ensemble average over the $N_r = 4$ or 6 realizations (for the vertical and horizontal measurements, respectively) and the temporal smoothing over $N_t = 1$ to 20 consecutive fields. The resulting number of samples ranges between 8×10^4 and 1.6×10^6. When there is no ambiguity, single brackets $\langle\cdot\rangle$ denote the three types of averages, and the root mean square (r.m.s.) is denoted as $A' = \langle A^2\rangle^{1/2}$. The convergence of the averages is determined by computing the standard deviation between the realizations. The standard deviation for the velocity statistics grows from 5 to 30 % during the decay (a wrong separation between the mean flow and turbulence increases the uncertainty when the scale of motion becomes larger than the field of view). The standard deviation for the velocity-gradient statistics is approximately 15 % throughout the decay, indicating that small-scale quantities are less affected by the mean-fluctuation decomposition of the flow.

3. Energy and integral scales

3.1. *Energy decay*

The time evolution of the streamwise velocity variance for the total flow, $\langle U_x^2\rangle$, and the turbulent flow, $\langle u_x^2\rangle = \langle (U_x - \langle U_x\rangle)^2\rangle$, are shown in figure 4. In the absence of rotation (figure 4*a*), the energy of the mean flow clearly dominates the total energy, by a factor up to 10 for $t \simeq 1000M/V_g$. On the other hand, when rotation is present (figure 4*b*), the turbulence energy is very close to the total energy, confirming that the mean flow is significantly reduced in the presence of rotation.

In the non-rotating case, once the mean flow is subtracted, the turbulent energy decays as t^{-n} up to $t \simeq 400M/V_g$, with $n \simeq 1.22 \pm 0.05$. This decay exponent turns out to be very close to the Saffman (1967) prediction $n = 6/5$ for unbounded turbulence (in the early stage of decay, the vertical confinement may indeed be neglected, as shown in § 3.3). The streamwise variance, $\langle u_x^2\rangle$, is approximately 1.4 times larger than the two spanwise variances $\langle u_y^2\rangle$ and $\langle u_z^2\rangle$, reflecting the usual residual anisotropy of grid turbulence (Comte-Bellot & Corrsin 1966). For $t > 400M/V_g$, the shallower decay probably originates from the turbulence production by the mean residual shear. This

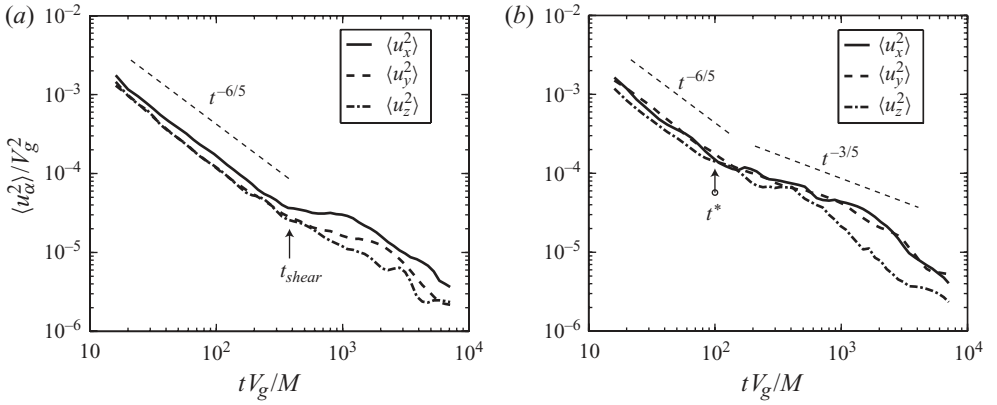

FIGURE 5. Time evolution of the variance of the three velocity components. The variances $\langle u_x^2\rangle$ and $\langle u_y^2\rangle$ are computed from the horizontal PIV fields (camera C1) and $\langle u_z^2\rangle$ from the vertical PIV fields (camera C2), for non-simultaneous experiments. (*a*) $\Omega = 0$. The arrow at t_{shear} indicates the time after which the turbulent energy production by the residual mean shear becomes significant. (*b*) $\Omega = 0.05\,\mathrm{rad\,s^{-1}}$. The arrow at t^* indicates the transition between the $t^{-6/5}$ isotropic decay and the $t^{-3/5}$ decay affected by the rotation.

transition time, denoted t_{shear} in figure 5(*a*), is indeed of the order of the shear time scale, $(\partial U_x/\partial z)^{-1} \simeq 250\,\mathrm{s}$. The ordering of the three velocity variances for $t \gg t_{shear}$, $\langle u_x^2\rangle > \langle u_y^2\rangle > \langle u_z^2\rangle$, actually confirms the shear-dominated nature of the turbulence in the non-rotating case at large times (Tavoularis & Karnik 1989).

In non-dimensional form, the decay law of the streamwise variance for isotropic turbulence is written (neglecting possible time origin shift)

$$\frac{\langle u_x^2\rangle}{V_g^2} \simeq A\left(\frac{tV_g}{M}\right)^{-6/5}. \tag{3.1}$$

A best fit for $t < t_{shear}$ yields a decay coefficient $A \simeq 0.045 \pm 0.005$, a value in good agreement with the literature for grid turbulence (Mohamed & LaRue 1990). This indicates that, in spite of the residual mean shear generated by the forcing, the decay of the turbulent kinetic energy is close to that of classical grid turbulence for $t < t_{shear}$, suggesting a negligible coupling between the mean flow and the small-scale turbulence at small time.

The time evolution of the three velocity variances in the rotating case is shown in figure 5(*b*) for $\Omega = 0.05\,\mathrm{rad\,s^{-1}}$. At early time, the three curves are very close to the reference case $\Omega = 0$ (figure 5*a*), confirming that the rotation has no measurable effect at large Rossby numbers. After a crossover time $t^* \simeq 100M/V_g$, the decay of the two horizontal variances $\langle u_x^2\rangle$ and $\langle u_y^2\rangle$ becomes shallower, showing a clear reduction of the energy decay by the rotation. On the other hand, the vertical variance $\langle u_z^2\rangle$ first follows the horizontal variance for a short time after the crossover time t^*, but sharply decreases soon after, reflecting a growth of anisotropy. Since here the turbulence production by the mean shear is essentially suppressed by the background rotation, this departure from the $t^{-6/5}$ decay and the resulting anisotropy growth can now be interpreted as a pure effect of the rotation.

3.2. *Crossover between the two decay regimes*

In order to characterize the influence of the rotation on the transition time t^*, the decays of the streamwise velocity variance $\langle u_x^2\rangle$ are compared in figure 6 for the four

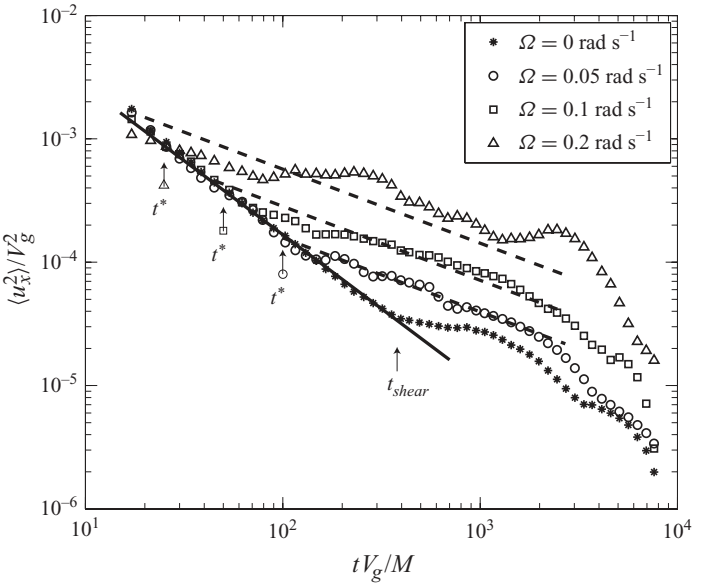

FIGURE 6. Time evolution of the streamwise velocity variance $\langle u_x^2 \rangle$, for the non-rotating and the three rotating experiments. The solid line shows $A(tV_g/M)^{-6/5}$ and the dashed lines show $A_\Omega Ro_g^{-3/5}(tV_g/M)^{-3/5}$. The transition between the non-rotating ($t^{-6/5}$) and rotating ($t^{-3/5}$) decay laws occurs at t^*, indicated by the three vertical arrows for each rotation rate. For $t > t_{shear}$ the turbulent energy production by the residual mean shear becomes significant in the non-rotating case.

sets of experiments. The crossover time t^* decreases from $100M/V_g$ to approximately $30M/V_g$ as Ω is increased, which turns out to be approximately 0.4 tank rotation. The small value of t^* found for the highest rotation rate indicates that the turbulent energy production in the wake of the grid may be indeed already affected by the background rotation in this specific case. The decay curve in this case is indeed particular, showing unexpected large fluctuations.

In the limit of large rotation rate, the energy decay can be modelled by assuming that the energy transfer rate scales as the linear time scale Ω^{-1}. Based on this argument, Squires *et al.* (1994) proposed, using dimensional analysis, the following asymptotic decay law:

$$\frac{\langle u_x^2 \rangle}{V_g^2} \simeq A_\Omega Ro_g^{-3/5} \left(\frac{tV_g}{M} \right)^{-3/5}, \tag{3.2}$$

with A_Ω being a non-dimensional constant. Although the elapsed time is moderate here, the decay curves in figure 6 are actually compatible with this shallower decay (3.2). Fitting the data for $\Omega = 0.05$ and $0.10\,\mathrm{rad\,s^{-1}}$ yields $A_\Omega \simeq 0.020 \pm 0.005$ (the data at $\Omega = 0.20\,\mathrm{rad\,s^{-1}}$ being excluded for the reason given before). Accordingly, the crossover time t^* between the non-rotating and the rotating decay laws is obtained by equating (3.1) and (3.2),

$$\frac{t^* V_g}{M} \simeq \left(\frac{A}{A_\Omega} \right)^{5/3} Ro_g \simeq (5 \pm 1) Ro_g, \tag{3.3}$$

yielding the values 100, 50 and 25 for the three rotation rates, which reproduce correctly the observed t^* (see the arrows in figure 6). Expressing this crossover

time (3.3) in terms of the rotation rate is consistent with a transition occurring at fixed fraction of tank rotation,

$$\frac{\Omega t^*}{2\pi} \simeq (5 \pm 1)/4\pi \simeq 0.4 \pm 0.1. \tag{3.4}$$

It is remarkable that the transition between the two regimes $t^{-6/5}$ and $t^{-3/5}$ is sufficiently sharp, so that the analysis of Squires *et al.* (1994) can be recovered to a correct degree of accuracy. A similar transition in the form $t^{-10/7} \to t^{-5/7}$, with again a factor 2 between the non-rotating and the rotating decay exponents, has been observed in the recent simulation of van Bokhaven *et al.* (2008), the discrepancy with the present exponents being probably associated with different energy content at small wavenumber.

3.3. *Integral scales*

We now turn to the time evolution of the integral scales in the horizontal plane, defined as

$$L_{\alpha\alpha,\beta}(t) = \int_0^{r^*} C_{\alpha\alpha,\beta}(r, t)\, \mathrm{d}r, \tag{3.5}$$

from the two-point correlation function of the α velocity component along the β-direction

$$C_{\alpha\alpha,\beta}(r, t) = \frac{\langle u_\alpha(\boldsymbol{x}, t) u_\alpha(\boldsymbol{x} + r\boldsymbol{e}_\beta, t)\rangle}{\langle u_\alpha^2 \rangle}. \tag{3.6}$$

The truncation scale r^* in (3.5) is defined such that $C_{\alpha\alpha,\beta}(r^*) = 0.2$. This truncation is introduced because of the poor convergence of the correlation for separations r approaching the image size. Although this definition systematically under-estimates the true integral scales (defined as $r^* \to \infty$), the trends observed from the truncated integral scales are expected to represent the evolution of the true ones. We first focus here on the horizontal scales, which is useful for the definition of the instantaneous Reynolds and Rossby numbers, and we describe the vertical scales in § 4.3.

The time evolution of the longitudinal integral scale, averaged over the two horizontal directions x and y (denoted here 1 and 2 by convention), $L_f = (L_{11,1} + L_{22,2})/2$, is plotted in figure 7. This integral scale shows little influence of the background rotation, in agreement with the observations of Jacquin *et al.* (1990), with $L_f(t) \simeq t^{0.35 \pm 0.05}$ for $t < 1000M/V_g$, for all rotation rates. The scatter at larger time is probably a consequence of the inadequate subtraction of the mean flow, which may occur when the size of the largest vortices becomes comparable to the imaged area.

Dimensional analysis actually predicts different growth laws for L_f in the non-rotating and rotating cases (Squires *et al.* 1994),

$$\left.\begin{aligned} \frac{L_f}{M} &\simeq B \left(\frac{tV_g}{M}\right)^{2/5} && (t \ll t^*), \\ \frac{L_f}{M} &\simeq B_\Omega Ro_g^{1/5} \left(\frac{tV_g}{M}\right)^{1/5} && (t \gg t^*), \end{aligned}\right\} \tag{3.7}$$

with B and B_Ω non-dimensional constants. Surprisingly, although the $t^{-6/5} \to t^{-3/5}$ transition at $t = t^*$ is evident in the energy decay curves (figure 6), there is no evidence for the equivalent $t^{2/5} \to t^{1/5}$ transition for L_f in figure 7. Within the experimental

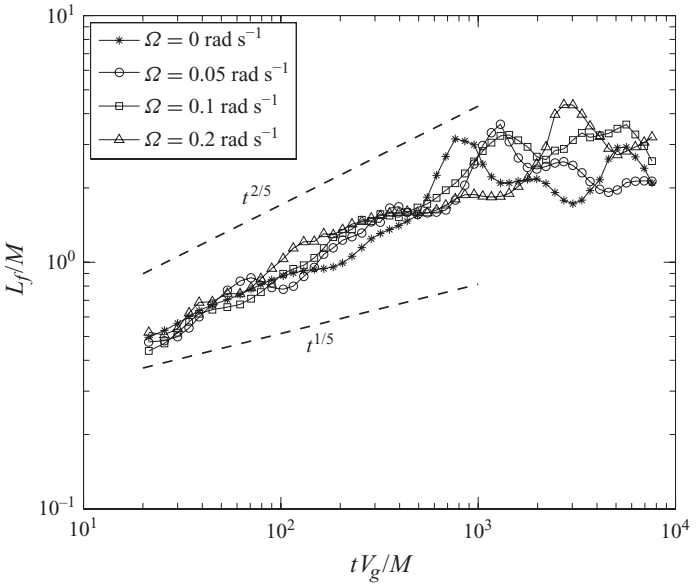

FIGURE 7. Time evolution of the longitudinal integral scale in the horizontal plane, $L_f = (L_{11,1} + L_{22,2})/2$, for the four series of experiments.

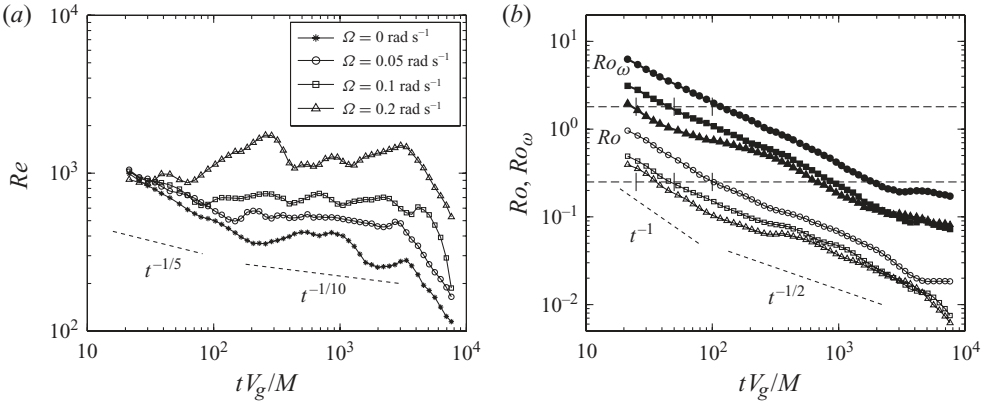

FIGURE 8. (*a*) Reynolds number $Re(t) = u'_x L_f/\nu$. (*b*) Micro- and macro-Rossby numbers, for the three experiments with background rotation. Upper curves (black symbols): $Ro_\omega = \omega'_z/2\Omega$. Lower curves (open symbols): $Ro = u'_x/2\Omega L_f$. The horizontal dotted lines show the thresholds, $Ro_\omega = 1.8$ and $Ro = 0.25$, with the corresponding transition times t^* indicated by the vertical ticks (see (3.3)).

uncertainty, a single power law $t^{2/5}$ actually provides a reasonable description for the growth of L_f both in the non-rotating and in the rotating cases.

3.4. *Instantaneous Reynolds and Rossby numbers*

The instantaneous Reynolds number, and the macro- and micro-Rossby numbers (Jacquin *et al.* 1990), are finally defined as

$$Re(t) = \frac{u'_x\, L_f}{\nu}, \quad Ro(t) = \frac{u'_x}{2\Omega\, L_f}, \quad Ro_\omega(t) = \frac{\omega'_z}{2\Omega}. \tag{3.8}$$

The time evolution of these numbers is plotted in figure 8(*a,b*). After a short period of sharp decay similar to the non-rotating case, the Reynolds number in the rotating cases shows a very weak decay in the range $t^* < t < 3000M/V_g$, ranging from 500 to 1300 as the rotation rate is increased. Also shown in this figure are the decay laws expected from (3.1), (3.2) and (3.7),

$$\left.\begin{aligned} Re(t) &\propto Re_g \left(\frac{tV_g}{M}\right)^{-1/5} && (t \ll t^*), \\ Re(t) &\propto Re_g Ro_g^{-1/10} \left(\frac{tV_g}{M}\right)^{-1/10} && (t \gg t^*). \end{aligned}\right\} \tag{3.9}$$

The micro-Rossby number, Ro_ω, shown in figure 8(*b*), takes values about 10 times larger than Ro throughout the decay (note that Ro_ω may be underestimated at small times because of the limited PIV resolution). This moderate ratio indicates that the range between the large scales dominated by the rotation and the small scales is indeed limited for the Reynolds number of the present experiments.

The joint decay and growth laws for the velocity and integral scale actually lead to a remarkably simple decay law for the macro-Rossby number $Ro(t)$. Combining again (3.1), (3.2) and (3.7) shows that, for $t < t^*$, the nonlinear time scale $\tau_{nl} = L_f(t)/u'_x(t)$ is simply proportional to the elapsed time, t, without dependence on the initial grid time scale M/V_g. As a consequence, the Rossby number $Ro = (2\Omega\tau_{nl})^{-1}$ is simply a function of the number of tank rotations,

$$\left.\begin{aligned} Ro(t) &\propto Ro_g \left(\frac{tV_g}{M}\right)^{-1} \propto (2\Omega t)^{-1} && (t \ll t^*), \\ Ro(t) &\propto Ro_g^{1/2} \left(\frac{tV_g}{M}\right)^{-1/2} \propto (2\Omega t)^{-1/2} && (t \gg t^*). \end{aligned}\right\} \tag{3.10}$$

At the transition $t = t^*$, which is reached after a fixed number of rotations, the Rossby number is indeed found approximately constant, $Ro(t^*) \simeq 0.25$ (see the vertical ticks at t^* in figure 8*b*). This value is in correct agreement with the transitional Rossby numbers reported by Hopfinger *et al.* (1982) and Staplehurst *et al.* (2008).

It is also of interest to characterize this transition in terms of the micro-Rossby number, $Ro_\omega(t)$, which is often used in the literature. For $t \ll t^*$, assuming again isotropic turbulence, the decay law of Ro_ω can be inferred from the relation between the vorticity r.m.s., the velocity r.m.s. and the dissipation rate,

$$\epsilon = -\frac{1}{2}\frac{\partial \boldsymbol{u}'^2}{\partial t} = -\frac{3}{2}\frac{\partial u'^2_x}{\partial t} = \nu\boldsymbol{\omega}'^2 = 3\nu\omega'^2_z. \tag{3.11}$$

Combining the isotropic decay law (3.1) with (3.11) gives

$$Ro_\omega(t) = \sqrt{\frac{3}{5}} A^{1/2} Re_g^{1/2} Ro_g \left(\frac{tV_g}{M}\right)^{-11/10} \qquad (t \ll t^*), \tag{3.12}$$

yielding a scaling exponent very close to that of $Ro(t)$. Evaluating Ro_ω at the transition $t \simeq t^*$, using (3.3), finally yields

$$Ro_\omega(t^*) \simeq \sqrt{\frac{3}{5}} (5 \pm 1)^{-11/10} A^{1/2} Re_g^{1/2} Ro_g^{-1/10}. \tag{3.13}$$

Accordingly, no strictly constant micro-Rossby number is expected at the transition, although the dependence on the rotation rate, as $\Omega^{1/10}$, is very weak (Ω is varied

by a factor of 4 only in the present experiment). As shown by the vertical ticks in figure 8(*b*), Ro_ω takes values which actually turn out to be approximately constant at the transition, $Ro_\omega(t^*) \simeq 1.8$. Interestingly, this value is close to the empirical threshold reported by Morize *et al.* (2005), below which the energy spectrum and the velocity derivative skewness were found to depart from the classical Kolmogorov predictions. Although the macro-Rossby number is probably a more relevant parameter to describe this transition, the similar Reynolds number of the two experiments explains the similar values of Ro_ω found at the transition.

4. Dynamics of the anisotropy

4.1. *Visualization of the vertical layers*

We now focus on the growth of anisotropy in the vertical plane (x, z). Figure 9 shows a sequence of six snapshots of the velocity field and spanwise vorticity, ω_y, after the transition $t > t^*$, for $\Omega = 0.20$ rad s^{-1} (see also supplementary movie 3). The anisotropy can be visually detected from the first snapshot, and the presence of vertical layers of ascending or descending fluid becomes evident after eight tank rotations (figure 9*c*). Lower rotation rates show similar layers (see also figure 2*d*), although thicker and less intense than for $\Omega = 0.20$ rad s^{-1}. These layers are difficult to infer from the velocity field itself, because of the superimposed strong horizontal flow, but they clearly appear through the surrounding layers of nearly constant ω_y of alternate sign. These layers of vertical velocity are consistent with a trend towards a three-component two-dimensional (3C2D) flow, with vanishing vertical variations of the velocity field, but non-zero vertical velocity u_z. Although compatible with the Taylor–Proudman theorem in an unbounded domain, this 3C2D flow organization is surprising here, because of the boundary layer conditions which should select a two-component two-dimensional flow (with $u_z = 0$). The persistence of these layers with non-zero u_z is discussed in § 4.4.

As time proceeds, the vertical layers become thinner and more vertically coherent (note that since only the intersection of the layers with the measurement plane can be visualized, the apparent thickness may overestimate the actual one). At large time (figure 9*e*,*f*), although these layers are nearly coherent from the bottom wall up to the free surface, they are not strictly vertical, but rather show wavy disturbances. These disturbances have amplitude and characteristic vertical size of the order of the layer thickness, suggesting the occurrence of a shear instability (discussed in § 4.5). We will examine in § 5 the consequence of this instability on the dynamics and statistics of the vertical vorticity field.

4.2. *Decay of the vertical velocity and anisotropy growth*

The time evolution of the vertical velocity variance, $u_z'^2 = \langle u_z^2 \rangle_{x,z,e}$, and the isotropy ratio, u_z'/u_x', plotted in figure 10(*a*,*b*), show a complex behaviour. Here, the spatial average is computed only in the core of the flow, excluding layers of thickness $0.1h$ near the bottom wall and the free surface. Similarly to the horizontal variance (see figure 6), the vertical variance for the rotating cases first departs from the reference curve $t^{-6/5}$ of the non-rotating case, and follows a shallower decay which is compatible again with a $t^{-3/5}$ law, at least during an intermediate range. Although the $t^{-6/5} \to t^{-3/5}$ transition is not as sharp as for the horizontal variance, perhaps because of the limited statistics achieved for the measurements in the vertical plane, the transition time is compatible with the one determined for $\langle u_x^2 \rangle$, corresponding to $\Omega t^*/2\pi \simeq 0.4$ tank rotation. After $\Omega t/2\pi \simeq 2$, the vertical variance follows a significantly faster decay,

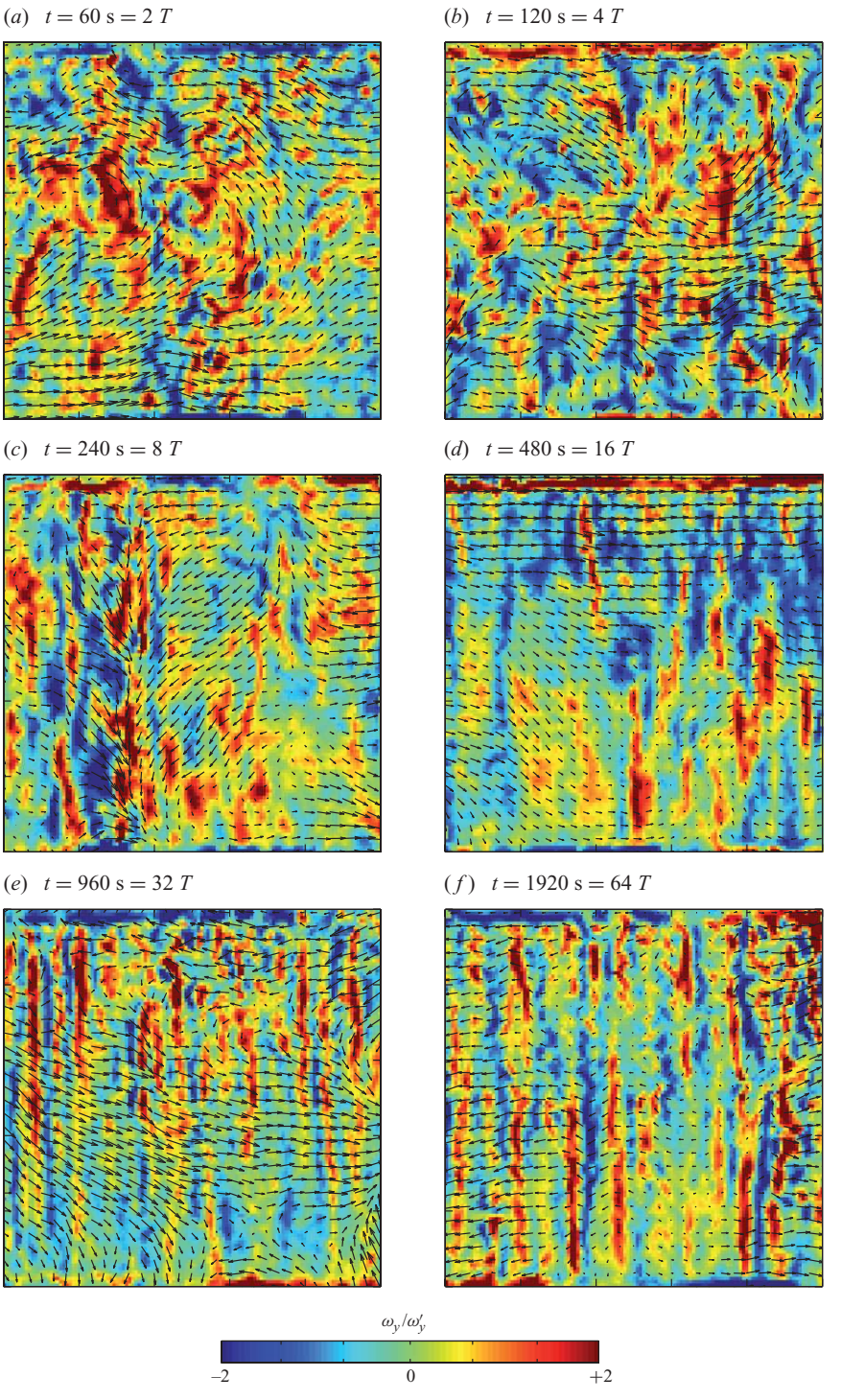

FIGURE 9. Sequence of six snapshots of the velocity and spanwise vorticity, ω_y, in the vertical plane (x, z) for $\Omega = 0.20$ rad s^{-1}. The imaged area is 1 m $\times$ 1 m. The grid is translated from left to right, and the time origin $t = 0$ is defined as the grid goes through the centre of the imaged area. The colour range is normalized by the r.m.s. ω'_y computed for each time.

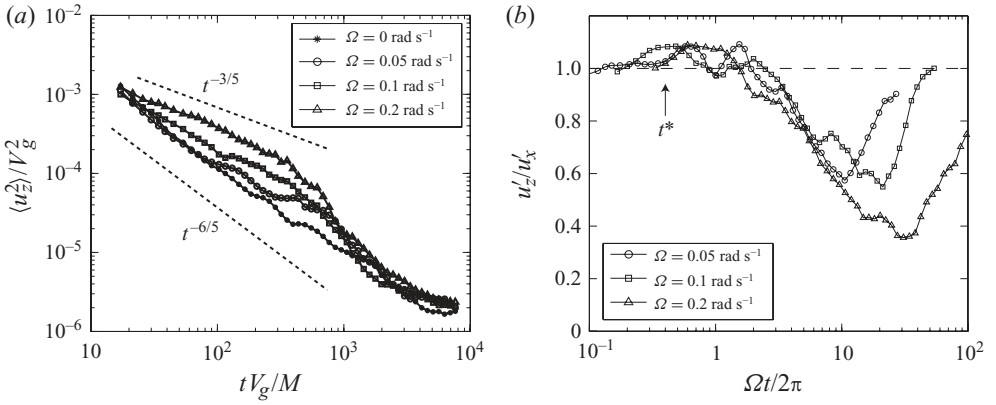

FIGURE 10. (*a*) Time evolution of the vertical velocity variance $\langle u_z^2 \rangle$, for the non-rotating and the three rotating experiments. (*b*) Isotropy factor u_z'/u_x' for the three rotating experiments, as a function of number of tank rotations. The vertical arrow indicates the transition between the $t^{-6/5}$ and the $t^{-3/5}$ decay regimes at $\Omega t^*/2\pi \simeq 0.4$.

whereas the horizontal variance still decays as $t^{-3/5}$, yielding a growing anisotropy in the vertical plane. Although the formation of vertical structures is evident in the spanwise vorticity field ω_y (figure 9), the anisotropy remains moderate when expressed in terms of the ratio of velocity variances. This ratio reaches a weak minimum between 0.6 ± 0.2 and 0.4 ± 0.15 only, after 10–30 tank rotations, depending on the rotation rate. This confirms that the velocity field remains significantly three-component, although the dynamics of the large scales becomes nearly two-dimensional (i.e. z-invariant). Interestingly, the ratio u_z'/u_x' for the different rotation rates collapses in the anisotropy growth regime when plotted as a function of the number of tank rotations $\Omega t/2\pi$.

An intriguing feature of figure 10(*b*) is the reverse trend $u_z'/u_x' \to 1$ observed at large time. This apparent return to isotropy is associated with the flattening of the decay of $\langle u_z^2 \rangle$ at large time, visible in figure 10(*a*). A similar behaviour is obtained for the Reynolds stress anisotropy in the numerical simulations of Morinishi, Nakabayashi & Ren (2001). It is in apparent contradiction with the clear anisotropy visible in figure 9(*e*,*f*), confirming that the ratio of velocity variances is not an appropriate indicator of anisotropy.

4.3. *Integral scales in the vertical plane*

In order to relate the evolution of the vertical velocity variance to the formation, thinning and instability of the vertical layers, we now focus on the statistical geometry of these layers. For this, we have computed the three integral scales $L_{11,3}$, $L_{33,1}$ and $L_{33,3}$, using definitions (3.5) and (3.6) with $\alpha, \beta = 1, 3$. $L_{11,3}$ characterizes the trends towards two-dimensionality, $L_{33,3}$ the vertical coherence of the layers and $L_{33,1}$ the thickness of the layers. No reliable measurement of $L_{11,1}$ could be obtained from the vertical fields, because of the ambiguity of the subtraction of the horizontal LSC flow at large time: large-scale vortices having their axis out of the measurement plane produce strong horizontal velocity which, if subtracted, yield an unphysical decrease of $L_{11,1}$. Here again, in (3.6), the depth-average excludes lower and upper layers over a thickness of $h/10$, in order to avoid boundary effects. In the extreme case of an unbounded z-invariant 2D flow, the vertical correlations would be $C_{\alpha\alpha,3}(r) = 1$, yielding $L_{\alpha\alpha,3} = \infty$.

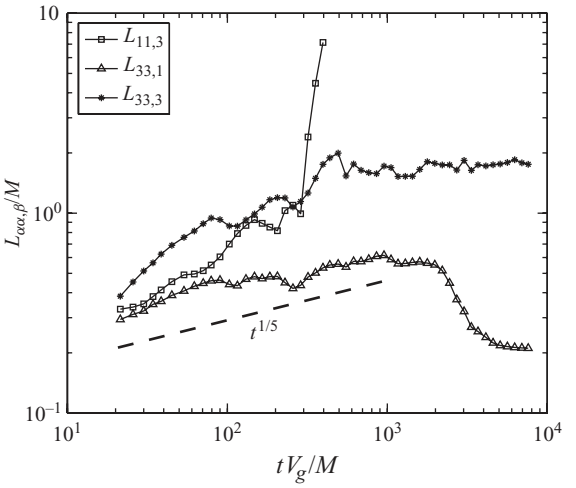

FIGURE 11. Time evolution of the normalized integral scales $L_{\alpha\alpha,\beta}/M$ computed in the vertical plane, for $\Omega = 0.10\,\mathrm{rad\,s^{-1}}$. For $tV_g/M > 400$, $L_{11,3}$ is no longer defined, because the correlation $C_{11,3}$ does not decrease sufficiently for large vertical separations.

The time evolution of the three integral scales is shown in figure 11, in the case $\Omega = 0.10\,\mathrm{rad\,s^{-1}}$. At short time, the longitudinal integral scale $L_{33,3}$ is, as expected, larger than the two transverse ones (one has $L_{33,3} = 2L_{11,3} = 2L_{33,1}$ for isotropic turbulence). The most spectacular effect is the rapid growth of $L_{11,3}$, characterizing the vertical correlation of the horizontal velocity, which is a clear signature of the two-dimensionalization of the large scales of the flow. However, this integral scale could not be computed for $tV_g/M > 400$ because the correlation $C_{11,3}(r)$ does not decrease below the chosen threshold 0.2. Although the limited range of rotation rate prevents a clear check of the scaling of this divergence time, we can note that it occurs roughly at a constant number of tank rotations. Assuming that energy is contained at scale $L_{11,1} \simeq M$ at early time, and that eddies grow vertically by wave propagation, $L_{11,3}$ is expected to increase by an amount of $L_{11,1}$ at each tank rotation. Accordingly, the divergence of $L_{11,3}$ is expected after a number of tank rotations of order of $h/M \simeq 7$, where h is the channel depth, in qualitative agreement with the present observations. After the divergence of $L_{11,3}$, the vertical correlation of the vertical velocity remains constant until the end of the experiment, with $L_{33,3} \simeq 2M$, indicating a significant, although finite, vertical coherence of the ascending and descending layers. Note that, however, even strictly coherent thin layers of constant velocity would lead to finite integral scale $L_{33,3}$, because the tilting of the layers by the oscillating shear of the IW flow strongly reduces the vertical correlation as the layers become thinner.

A remarkable feature of figure 11 is the sharp decrease of the horizontal correlation of the vertical velocity, described by $L_{33,1}$, for $tV_g/M > 2000$ (corresponding to $\Omega t/2\pi \simeq 16$–24 tank rotations), and its subsequent saturation to the very low value $L_{33,1} \simeq 0.2M \simeq 30\,\mathrm{mm}$ at large time. In the final stage of the decay, the strong anisotropy is characterized by the following non-trivial ordering (see figures 7 and 11):

$$L_{33,1} \ll L_{33,3} \simeq L_{11,1} \ll L_{11,3}. \tag{4.1}$$

The low asymptotic value of $L_{33,1}$ suggests that, in the final regime, the vertical-velocity fluctuations have a well-defined characteristic scale in the horizontal direction,

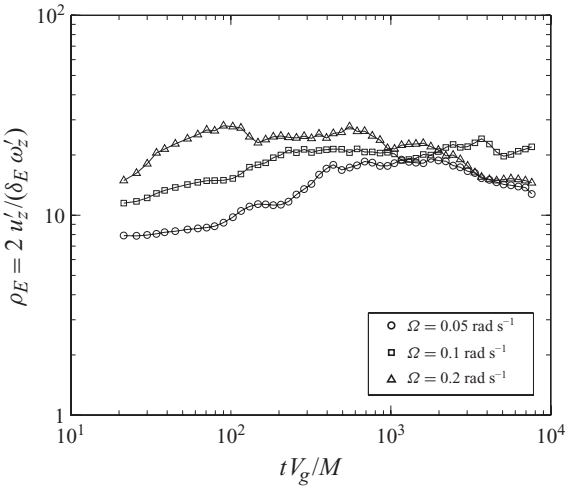

FIGURE 12. Time evolution of the Ekman ratio, ρ_E, (4.2), showing that the vertical velocity variance is significantly larger than the expected Ekman-pumping velocity.

i.e. there is no global vertical motion at scales larger than the thickness of the layers. This final value of $L_{33,1}$, which provides an estimate for the average thickness of the layers, is found to slightly decrease, from $0.23M$ to $0.17M$, as Ω is increased, suggesting that the thinning of the layers induced by the horizontal straining motion due to the large-scale vortices is stronger at higher rotation rate.

4.4. *Origin of the vertical layers*

Figure 10 raises the issue of the origin of the non-negligible vertical-velocity fluctuations found at large time. Although the Taylor–Proudman theorem predicts a 3C2D flow in the limit of low Rossby numbers, boundary conditions at $z = 0$ and h should actually select a 2D2C flow with zero vertical velocity at large time, apart from weak Ekman-pumping effects.

We can first note that the measured vertical velocity variance, even at large time, remains comfortably larger than the one expected for the Ekman pumping induced by the horizontal flow. According to the linear-Ekman-pumping theory, a quasi-2D field of vertical vorticity r.m.s., ω'_z, should lead to a characteristic vertical-velocity r.m.s. of $u'^E_z = \delta_E \omega'_z/2$ for $z \simeq \delta_E$ (Greenspan 1968), where δ_E is the Ekman-layer thickness (see § 2.2). The discrepancy between the actual u'_z and the Ekman-pumping estimate, u'^E_z, may be therefore measured by the ratio

$$\rho_E = \frac{2u'_z}{\delta_E \omega'_z}. \tag{4.2}$$

In figure 12, this ratio starts from about 10 at small time, and slightly increases up to about 20 at larger time, confirming that the Ekman pumping can be neglected in the present experiments.

Another possibility for this vertical velocity is the onset of a residual thermal convection motion at large time. Although the mixing induced by the grid translation homogenizes the flow temperature, a slight cooling of an upper layer of water may be induced by the evaporation, triggering convection cells in the depth of the channel. Although this effect cannot be ruled out in the present experiments, we note that such convection cells are not visually detected at the end of the decay for $\Omega = 0$, so

we believe that, if present, thermal convection should not play a significant role for $\Omega \neq 0$.

A remaining possibility for the vertical velocity found at large time is the initial vertical fluctuations induced by the grid. The 2D2C selection by the boundary conditions should be at work only after a sufficient time for the boundary conditions to influence the interior of the flow, and this time is apparently not reached in our experiments. Three relevant time scales may be considered for this problem: the vertical advection time, $\tau_h = h/u'_z$, the viscous time across the layer thickness, $\tau_v = L^2_{33,1}/\nu$, and the recirculation time in the Ekman boundary layers (Ekman time), $\tau_E = h/(\nu\Omega)^{1/2}$. In our experiment, at large times ($tV_g/M > 2000$), all the three time scales are found of the same order: $\tau_h \simeq 2000$ s (from figure 10*a*), $\tau_v \simeq 1000$ s (from figure 12) and $\tau_E \simeq 2000$–4000 s (see table 1). Since the three time scales are of the order of the experiment duration itself (3600 s), it is conceivable that the boundary conditions are only marginally felt by the vertical velocity in the shear layers. Accordingly, these layers may be seen as a vestige of early vertical fluctuations induced by the grid and advected by the horizontal large-scale flow, suggesting that even longer experiments would be necessary to observe the selection of a pure 2D2C flow.

4.5. *Stability of the vertical layers*

Although the strong anisotropy of the flow in the final stage is well characterized by the ordering of the the integral scales (4.1), the ratio of the velocity variances remains close to 1 (figure 10*b*). More surprisingly, the quasi-isotropy of the velocity also holds at small scales, as shown by the following two velocity gradient isotropy factors:

$$\frac{\omega'_y}{\omega'_z} \quad \text{and} \quad \sqrt{5}\frac{\gamma'_z}{\omega'_z}, \tag{4.3}$$

where $\gamma'_z = \langle(\partial u_z/\partial z)^2\rangle^{1/2}$ is the r.m.s. of the vertical strain rate. The vertical strain rate plays an important role, as it is responsible for the stretching of the absolute vertical vorticity. In isotropic turbulence, both quantities are equal to 1 (the second equality follows from the classical isotropic relation $\epsilon = 15\nu\gamma'^2_z = \nu\boldsymbol{\omega}'^2 = 3\nu\omega'^2_z$, where ϵ is the dissipation rate). For a 2D flow with arbitrary vertical velocity, one has $\gamma_z = 0$, whereas $\omega_y = 0$ is true only for a two-dimensional two-component flow. As a consequence, the two isotropy factors may be considered as signatures of the *dimensionality* and *componentality* of the small scales, respectively (Cambon, Mansour & Godeferd 1997).

Figure 13 shows that the two velocity gradient isotropy factors first slowly decrease according to the linear time scale Ω^{-1}, reaching a moderate minimum of about 0.5 at the largest rotation rate. The time of maximum anisotropy for these quantities is close to that for u'_z/u'_x, and here again the collapse of the curves with respect to the linear time scale no longer applies during the increase at large time. This plot shows that, in the final stage, the small scales are both 3D and 3C, although not necessarily isotropic.

Assuming that the vertical velocity, u_z, behaves as a scalar field passively advected by the large-scale horizontal flow, provides a qualitative explanation for the increase of ω'_y/ω'_z at large time. As shown in figure 14(*a*), a layer of ascending fluid $u_z > 0$ in a horizontal strain field, for instance in the vicinity of a large vortex, is elongated along one direction and compressed along the other one, so it becomes thinner. In this process, u_z is approximately conserved, but its horizontal gradient $\nabla_h u_z$ increases, producing horizontal vorticity ω_x and ω_y which may reach, and even exceed, the vertical vorticity, ω_z.

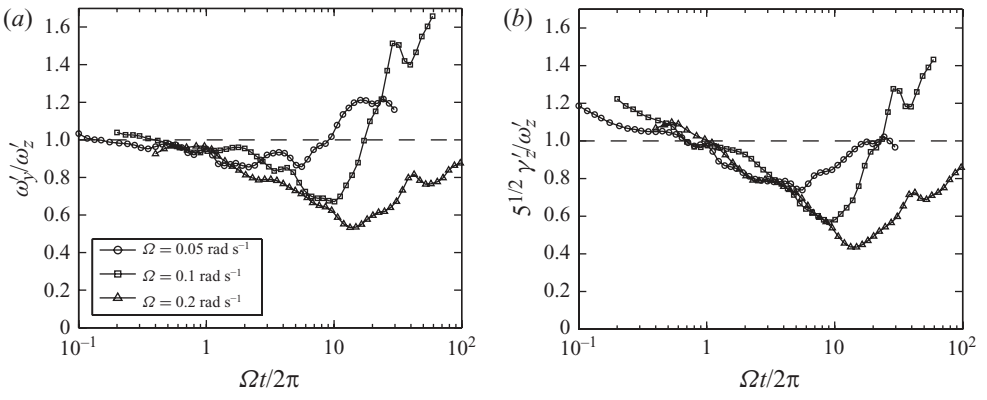

FIGURE 13. Time evolution of the velocity gradient isotropy factors: (*a*) ω_y'/ω_z' and (*b*) $\sqrt{5}\gamma_z'/\omega_z'$. In each figure, the horizontal dashed line indicates the isotropic values, $\omega_y'/\omega_z' = \sqrt{5}\gamma_z'/\omega_z' = 1$.

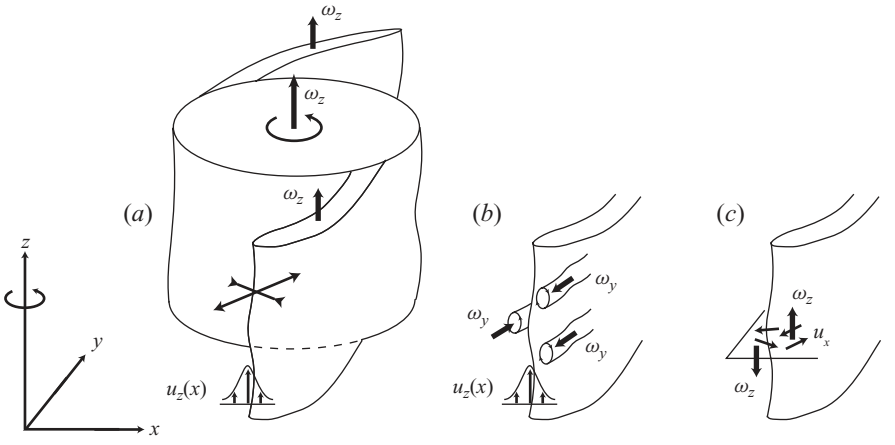

FIGURE 14. Sketch showing the thinning and instability of the vertical layers of vertical velocity advected by the horizontal flow. (*a*) Nearly vertical layer of ascending fluid, $u_z > 0$, strained in the vicinity of a large cyclone $\omega_z > 0$. (*b*) The layer becomes unstable, producing horizontal vortices. (*c*) These horizontal vortices produce random horizontal motion, and hence vertical vorticity of arbitrary sign.

The increase in γ_z', on the other hand, may be a consequence of the instability of these vertical layers. If the inertial time scale of the jets, $(\nabla_h u_z)^{-1} \simeq L_{33,1}/u_z'$, remains smaller than the dissipation time scale, $L_{33,1}^2/\nu$, the jets may undergo shear instabilities, producing horizontal vortices (sketched in figure 14*b*), as suggested by the visualizations in figure 9(*e*,*f*). This condition is actually satisfied: the Reynolds number, Re_l, based on these layers, defined as the ratio of the two time scales, is written

$$Re_l = \frac{L_{33,1}u_z'}{\nu} = \frac{L_{33,1}}{L_f}\frac{u_z'}{u_x'}Re, \tag{4.4}$$

where Re is the instantaneous Reynolds number defined in (3.8). With $L_{33,1}/L_f \simeq 0.1$, $u_z'/u_x' \simeq 0.5$, and Re ranging between 300 and 1300 in the final period of the decay

(see figure 8), one has $Re_l \simeq 10$–10^2, which is actually sufficient for a shear instability to develop. Little influence of the background rotation is expected on this shear instability, since the vertical velocity is unaffected by the Coriolis force (the resulting instability pattern, involving horizontal velocity, may, however, be affected by the rotation). The resulting wavy layers break the vertical invariance of u_z, thus producing vertical strain γ_z' of the order of the vorticity ω_y', in agreement with figure 13.

All these results suggest that the flow structure at large time is fully three-dimensional and three-component, with isotropy factors (4.3) close to that of 3D isotropic turbulence, although the large scales are highly anisotropic, as described by the ordering of the integral scales (4.1).

5. Cyclone–anticyclone asymmetry

5.1. *Dynamics of the cyclones and anticyclones*

We finally turn to the structure of the vertical vorticity field in the rotating case, focusing on the issue of the cyclone–anticyclone asymmetry. The dynamics of the horizontal flow is illustrated by six snapshots in figure 15 for $t > t^*$ (see also the supplementary movie 2). At the beginning of the decay, the vorticity field consists of small-scale disordered fluctuations (figure 15*a*,*b*), which gradually evolve into a complex set of tangled vortex sheets and vortices (figure 15*c*). A set of well defined, nearly circular, cyclones gradually emerges and separates from the turbulent background (figure 15*d*). Anticyclones are also encountered, but they are weaker and less compact than the cyclones. Once formed, visual inspections of the movies indicate that the anticyclones are not specifically unstable compared to the cyclones. This observation suggests that the cyclone–anticyclone asymmetry originates essentially from an enhanced vortex stretching of the cyclonic vorticity operating at early time, and not from a preferential instability of the anticyclones at large time.

At large time, the size of the cyclones grows, and merging of cyclones is frequently encountered, as illustrated in figure 15(*e*). No event of anticyclone merging is observed, probably because of their too small density. At the same time, a background of small-scale-vorticity fluctuations of random sign appears (figure 15*e*,*f*) and, at the end of decay, the flow essentially consists of these small-scale symmetric fluctuations advected by the large scale, mostly cyclonic, vortices.

5.2. *Growth of vorticity skewness*

The gradual structuring of the vorticity field is described by the vorticity skewness and flatness factors,

$$S_\omega = \frac{\langle \omega_z^3 \rangle}{\langle \omega_z^2 \rangle^{3/2}}, \quad F_\omega = \frac{\langle \omega_z^4 \rangle}{\langle \omega_z^2 \rangle^2} \tag{5.1}$$

(where the brackets denote horizontal and ensemble average), which are plotted in figure 16. Both S_ω and F_ω show a non-monotonic behaviour, with a collapse in the growth regime when plotted as a function of the number of tank rotations $\Omega t/2\pi$. Note that the residual oscillations visible at small times are associated with the large-scale IW flow (see § 2.4), of period $\Omega t/2\pi = 1/2$. As for the isotropy factors, the re-scaling with Ω^{-1} no longer holds during the decrease of S_ω and F_ω at large time.

For $t < t^*$, the vorticity skewness, S_ω, is essentially zero, within an uncertainty of $\pm 10^{-1}$. For $t > t^*$, it grows according to the power law

$$S_\omega \simeq 0.45 \left(\frac{\Omega t}{2\pi} \right)^{0.7}, \tag{5.2}$$

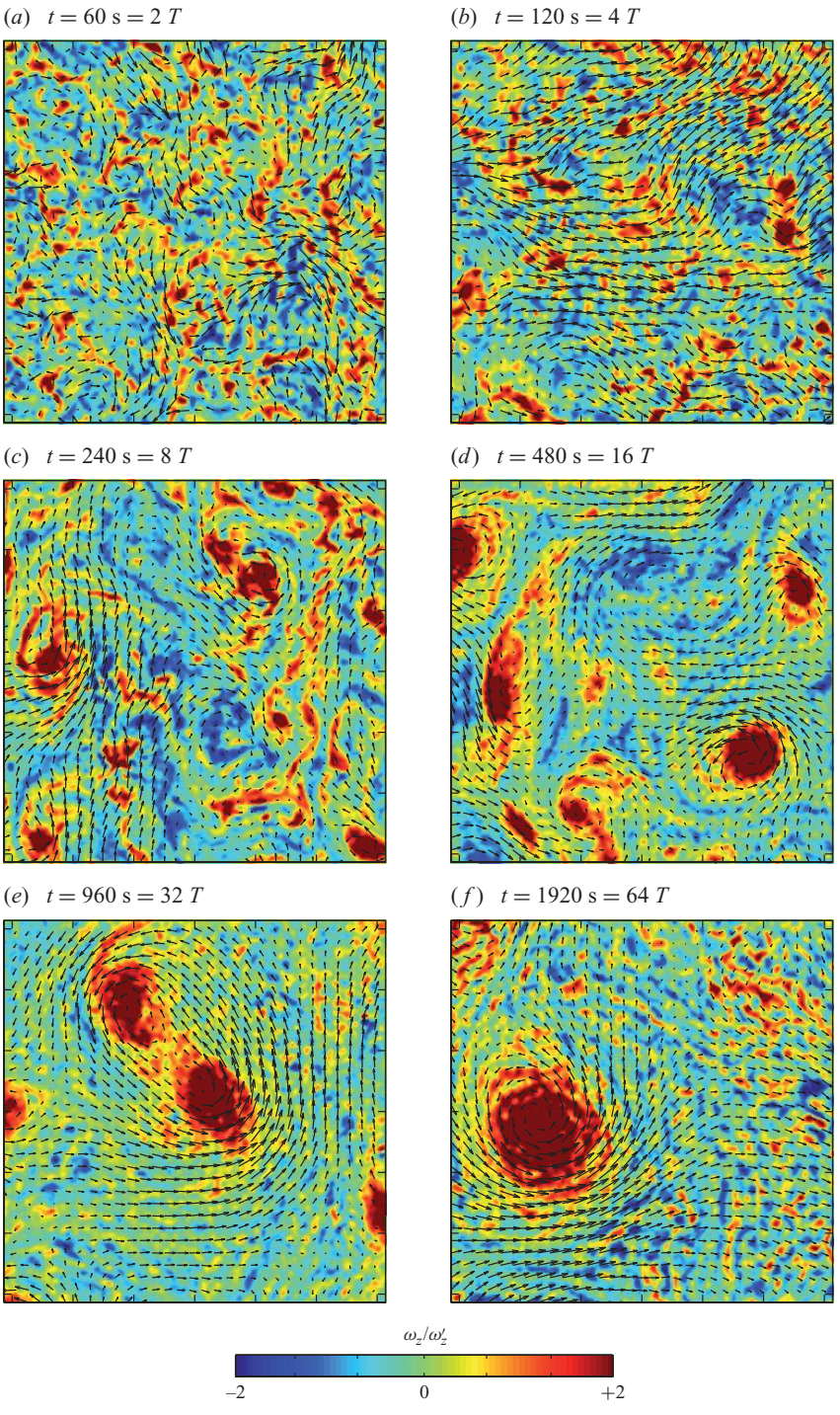

FIGURE 15. Sequence of six snapshots of the velocity and vertical vorticity fields, ω_z, measured in a horizontal plane (x, y) at mid-height for $\Omega = 0.20$ rad s^{-1}. The imaged area is 1.3 m $\times$ 1.3 m, representing 4.6 % of the tank section. The tank rotation is anticlockwise. Positive and negative vorticity indicate cyclones (in red) and anticyclones (in blue), respectively. The colour range is normalized by the r.m.s. ω'_z computed for each time.

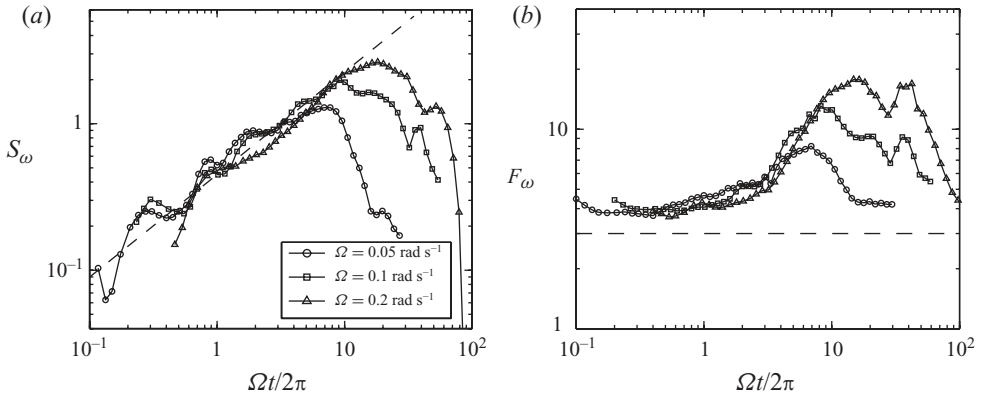

FIGURE 16. Vorticity skewness, S_ω, and (b) vorticity flatness, F_ω, as a function of the number of tank rotation $\Omega t/2\pi$. In (a), the dashed line shows the fit $0.45(\Omega t/2\pi)^{0.7}$. In ($b$), the dashed line indicates the value $F_\omega = 3$ corresponding to a Gaussian field.

which is in remarkable agreement with the one reported by Morize *et al.* (2005), both concerning the exponent and the numerical pre-factor. Although in both experiments turbulence is generated by the translation of a grid, the details of the geometry differ in a number of respects: here the grid velocity is normal to the rotation axis and the aspect ratio is significantly lower ($h/L_y = 0.25$ instead of 1.3). The collapse of S_ω for the two experiments is a clear indication of a generic behaviour of this quantity in decaying rotating turbulence (Morize *et al.* 2006*b*).

The peak values of S_ω, between 1.5 and 3 for increasing Ω, are significantly larger than those obtained in the experiments of Morize *et al.* (2005) and Staplehurst *et al.* (2008), and in the direct numerical simulation of van Bokhoven *et al.* (2008). The corresponding peaks of F_ω, between 8 and 18, are much larger than usually measured in non-rotating turbulence at similar Reynolds number (see e.g. Sreenivasan & Antonia 1997), an indication of the strong concentration of vorticity in the core of the cyclones.

5.3. *The decay of vorticity skewness at large time*

For larger times, when the flow consists mostly of isolated large-scale cyclones, S_ω starts decreasing back to zero, while F_ω recovers values around four, similar to the beginning of the decay. The important scatter in the decay is due to the limited sampling: at large times, the number of strong vortices per unit of imaged area is of order of 1, so the statistics become very sensitive to events of vortices entering or leaving the field of view.

There is no general agreement concerning the decrease of S_ω at large time. It was attributed to confinement effects by Morize *et al.* (2005), namely the diffusion induced by the Ekman pumping on the cyclonic vortices. This suggestion was motivated by the fact that the time t_{max} of maximum S_ω was approximately following the Ekman time scale, $t_{max} \simeq 0.1h(\nu\Omega)^{-1/2}$. Fitting the times of maximum skewness for the present data would actually give similar values, although the spread of the maximum of S_ω and the limited range of Ω prevent a clear check of the $\Omega^{-1/2}$ scaling here. However, the fact that the Ekman pumping is shown to have no significant effect in the present experiment (see § 4.4) makes this interpretation questionable. The role of the confinement in the decay of S_ω is also questioned by the numerical data of van Bokhoven *et al.* (2008), who have reported a decrease of S_ω at large times

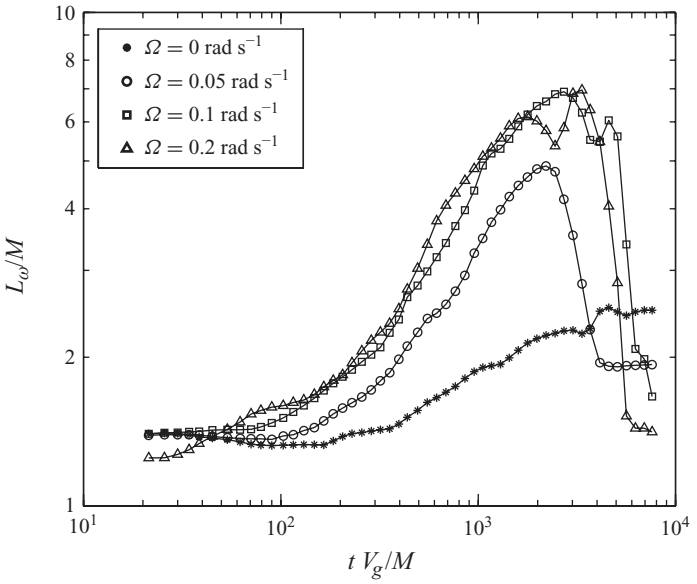

FIGURE 17. Time evolution of the horizontal integral scale of vertical vorticity, L_ω.

in a homogeneous turbulence with periodic boundary conditions, and hence without Ekman pumping. Note that no decrease in S_ω was reported in the numerical simulation of Bourouiba & Bartello (2007) and in the experiment of Staplehurst *et al.* (2008), perhaps because of their limited temporal range. The measurements of the latter were restricted to three tank rotations, whereas the decrease of S_ω starts typically after 10 rotations here and in Morize *et al.* (2005).

Apart from diffusion effects, another possible contribution for the decrease in S_ω is based on the fact that vorticity is a small-scale quantity, whereas the cyclone–anticyclone asymmetry is defined by structures of increasing size as time proceeds. In particular, it is observed that the flow outside the cyclones is not smooth, but is made of small scale, approximately symmetric, vorticity fluctuations. These vorticity fluctuations could originate from the instabilities of the vertical shear layers strained by the horizontal large-scale flow, as described in § 4.5. The horizontal vortices resulting from this instability induce a horizontal straining flow (figure 14*b*), which may itself be unstable and produce vertical vorticity of random sign at small scale (figure 14*c*). Accordingly, there is a possibility for the vorticity skewness to return to zero at large time, although the large-scale field remains dominated by a set of large cyclones.

The characteristic size of the vortical structures may be estimated from the horizontal integral scale of the vertical vorticity, $L_\omega = (L^\omega_{33,1} + L^\omega_{33,2})/2$. Here the integral scales for the vorticity are defined similarly to those for the velocity, by modifying (3.5) as

$$L^\omega_{33,\beta} = \int_0^{r^*} \frac{\langle \omega_z(\boldsymbol{x}, t)\omega_z(\boldsymbol{x} + r\boldsymbol{e}_\beta, t)\rangle}{\langle \omega_z^2 \rangle}\,\mathrm{d}r \tag{5.3}$$

(note that the truncation scale r^* is not essential here, because the vorticity correlation decreases sufficiently rapidly). Figure 17 shows the characteristic increase and decrease of L_ω when rotation is present, whereas it monotonically increases in the absence of rotation. The decrease occurs at $tV_g/M \simeq 2000$ for all rotation rates, which

coincides with the sharp decrease in $L_{33,1}$ (figure 11) and the isotropy factors (figure 13), and L_ω reaches values of order $0.2M \simeq 30\,\mathrm{mm}$, similar to those found for $L_{33,1}$. This suggests that the vertical vorticity field is dominated, at large time, by the small-scale fluctuations induced by the instabilities of the vertical shear layers.

The role of the symmetric small-scale vorticity fluctuation in the decrease in S_ω must be addressed carefully, because the vorticity field computed from the PIV is affected by measurement noise. If we assume that the PIV noise can be simply described as an additive symmetric noise, it should imply a trivial reduction of S_ω. This is a delicate issue, because the scale L_ω of these vorticity fluctuations is only slightly larger than the PIV resolution (§ 2.2). However, the temporal coherence of these small-scale fluctuations advected by the large scales is evident at the end of the supplementary movie 2, whereas PIV noise would generate vorticity patterns essentially uncorrelated in time. The temporal coherence of the fluctuations may also be inferred from the four snapshots shown in figure 18, where sets of arbitrary chosen vorticity patterns (marked in dashed ellipses) can be easily tracked in time, confirming that they are essentially advected by the large-scale motions.

5.4. *Skewness of the filtered vorticity field*

In order to characterize more precisely the influence of the measurement noise on the vorticity statistics, we have computed S_ω from the filtered velocity $\tilde{\boldsymbol{u}}$ obtained by convolution of $\boldsymbol{u}$ with a Gaussian kernel of size r_f,

$$\tilde{\boldsymbol{u}}(x, y, t; r_f) = \iint \boldsymbol{u}(x', y', t) \frac{1}{2\pi r_f^2} \mathrm{e}^{-((x-x')^2+(y-y')^2)/2r_f^2}\, \mathrm{d}x'\, \mathrm{d}y'. \tag{5.4}$$

In practice, the integral is restricted to a square of size $6r_f$.

The time evolution of the skewness of the filtered vorticity, $S_{\tilde{\omega}}$, is shown in figure 19(a) for various filter sizes r_f, in the case $\Omega = 0.20\,\mathrm{rad\,s^{-1}}$. In the growth regime, increasing the filter size leads to a decrease in S_ω, showing that the vorticity asymmetry is essentially contained at the smallest scales. In this situation, although the measured S_ω may underestimate the actual one because of the finite resolution of the PIV measurement, the vorticity skewness truly reflects the cyclone–anticyclone asymmetry at the smallest scales. On the other hand, after the peak of S_ω, the ordering of the curves is reversed, so that filtering the vorticity field now increases the skewness, showing that now the asymmetry is carried by vortices at larger scales. This is consistent with figure 18, where a large cyclone containing small-scale vorticity fluctuations is shown (white circle). However, it must be noted that although the peak of S_ω is shifted to larger times, a decrease in S_ω is still observed. The effect of the filtering is further illustrated in figure 19(b), where $S_{\tilde{\omega}}$ monotonically decreases as r_f is increased at $t = 8T$, whereas it shows a non-monotonic behaviour at $t = 90T$. Interestingly, in this latter case, the filter size for which $S_{\tilde{\omega}}$ is maximum at a given time provides a rough estimate of the size of the vortices responsible for the cyclone–anticyclone asymmetry.

One may conclude that, although S_ω provides a suitable description of the vorticity asymmetry during the growth regime, when the characteristic size of the vortices corresponds to the diffusive scale (the 'Kolmogorov scale' modified by the rotation), it is no longer appropriate as the vortex size grows at larger time, and in that case S_ω is strongly reduced by the small-scale symmetric vorticity fluctuations. This does not imply, however, that filtering at even larger scales would totally inhibit the decrease

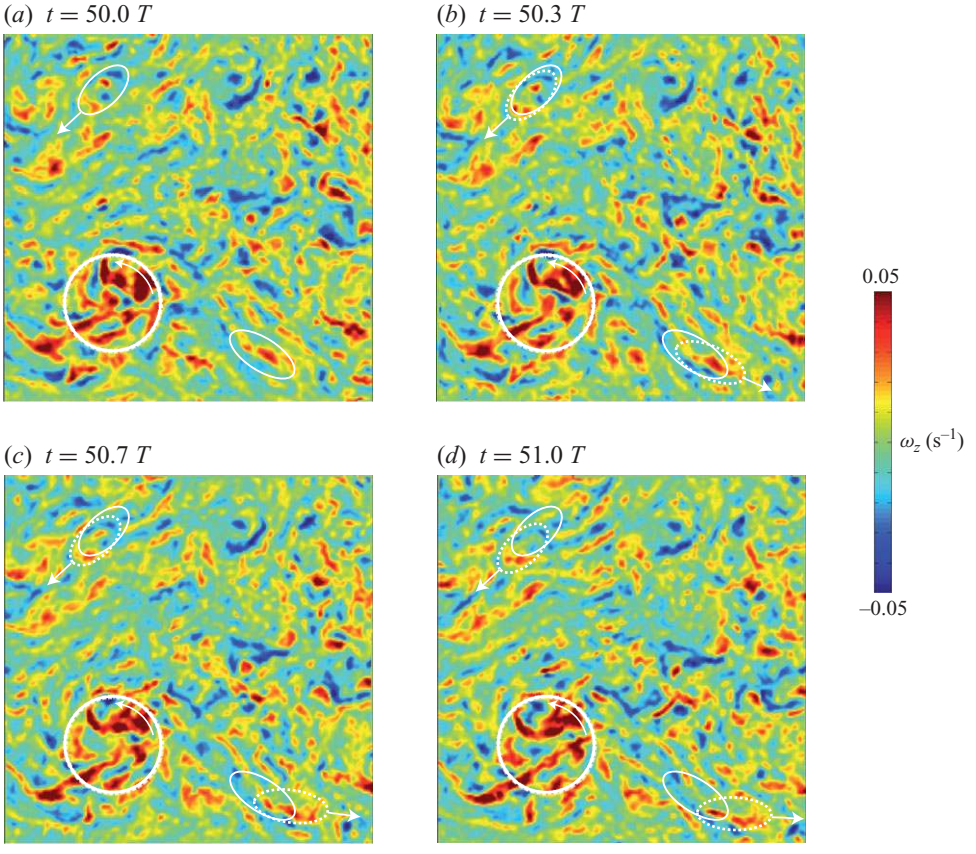

FIGURE 18. Sequence of four ω_z-snapshots in the horizontal plane (x, y) at large time, showing the advection of the small-scale symmetric vorticity by the large-scale horizontal motion ($\Omega = 0.10\,\mathrm{rad\,s^{-1}}$, $t \simeq 64M/V_g$). Each image is separated by $20\,\mathrm{s} = T/3$, and the field of view is $1.3\,\mathrm{m} \times 1.3\,\mathrm{m}$. The two ellipses track some arbitrary vorticity pattern in time. The angular velocity of the cyclonic structure in (*c*) (white circle) is $\Omega_c \simeq 0.009\,\mathrm{rad\,s^{-1}}$, corresponding to a local Rossby number of $\Omega_c/\Omega = 0.09$.

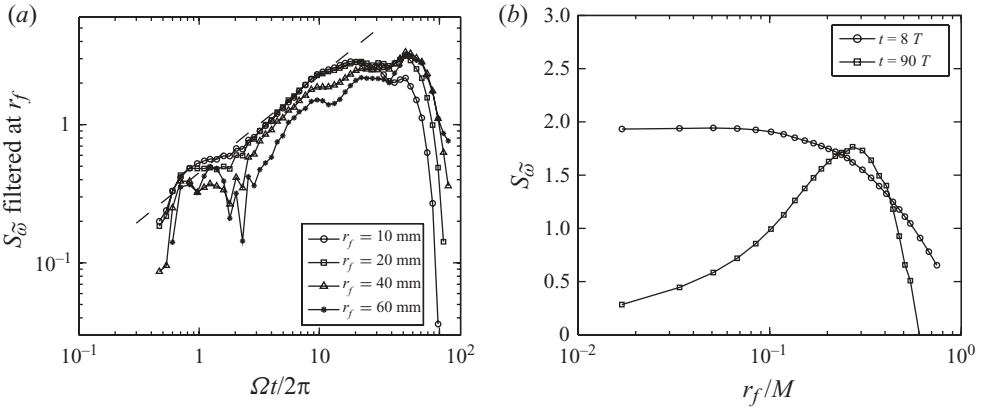

FIGURE 19. (*a*) Time evolution of the skewness of the filtered vorticity field, $S_{\tilde{\omega}}$, for different filter size, r_f, for $\Omega = 0.20\,\mathrm{rad\,s^{-1}}$. (*b*) Vorticity skewness as a function of the filter size, at times $t = 8T$ (before the peak of S_ω) and $t = 90T$ (after the peak).

of S_ω, since dissipation (either bulk viscous dissipation or through Ekman pumping) may be also responsible for the reduction in S_ω.

A more suitable statistical quantity, based for instance on the transverse velocity increments, should provide a better description of the cyclone–anticyclone asymmetry at large time. A vortex census approach, such as introduced in 2D turbulence (McWilliams 1990) would also help to decide which contribution dominates the decrease in S_ω. This approach is, however, difficult with the present data, because at large time the average number of vortices per field of view is of the order of or less than one.

6. Conclusion

The present experiment aims to focus on the transition at Rossby number $Ro \simeq O(1)$ which occurs in the course of the decay of grid turbulence, initially approximately homogeneous and isotropic, in a rotating frame. Emphasis is on the energy decay, anisotropy growth and asymmetry between cyclonic and anticyclonic vorticity. The different steps of the decay can be summarized as follows.

(*a*) During the first 0.4 tank rotation (between $25M/V_g$ and $100M/V_g$), the instantaneous Rossby number, Ro, is larger than 0.25 and turbulence is essentially unaffected by the background rotation. Once the large-scale mean flow and inertial oscillations are subtracted, the turbulent energy decays similarly to the classical $t^{-6/5}$ law of isotropic unbounded turbulence.

(*b*) After 0.4 tank rotation, $Ro < 0.25$, and the first effects of the rotation are triggered. Provided the grid Rossby number is large enough, the energy decay in this regime is found to be compatible with the $\Omega^{3/5}t^{-3/5}$ law proposed by Squires *et al.* (1994). Both the large-scale isotropy factor u'_z/u'_x and the small-scale ones ω'_y/ω'_z and γ'_z/ω'_z depart from their isotropic value, although reaching only a moderate value of about 0.5. On the other hand, the integral scales become strongly anisotropic, with a marked vertical correlation of the horizontal velocity. A cyclone–anticyclone asymmetry develops by preferential vortex stretching of the cyclonic vorticity, and is well described by a power-law growth of the vorticity skewness as $S_\omega \propto (\Omega t)^{0.7}$, consistent with the previous findings of Morize *et al.* (2005).

(*c*) Finally, a last regime is observed for $t > 2000M/V_g$ (corresponding to 10–30 tank rotations), in which the spanwise vorticity field is dominated by thin layers, which are prone to shear instabilities. These instabilities produce small-scale spanwise vorticity, resulting in an apparent return to isotropy for the ratio of the velocity or vorticity components. However, the flow structure remains strongly anisotropic, as revealed by the characteristic ordering of the integral scales. A remarkable consequence of the instability of these vertical shear layers is that it re-injects horizontal velocity disturbances, and hence vertical vorticity with random sign, at small scales.

The mechanism of re-injection of symmetric vorticity fluctuations in the last regime is found to contribute significantly to the reduction of the vorticity skewness, S_ω, although the large-scale vortices still remain preferentially cyclonic. These results suggest that the 2D versus 3D nature of the initial conditions have a critical importance in the asymptotic state of decaying rotating turbulence. For initial isotropic turbulence, as is approximately produced in the wake of a grid, the initial vertical fluctuations, which represent $1/3$ of the initial turbulent kinetic energy, are temporarily stored by the horizontal quasi-2D motions and play no role in its dynamics at intermediate time. However, the energy of these vertical fluctuations may be released directly at small scale via the shear instability mechanism of the vertical layers at large time, resulting in a shortcut of the energy cascade. A rather different situation is

expected for decaying rotating turbulence starting from strictly 2D initial conditions, as in the experiments of Longhetto *et al.* (2002) and Praud *et al.* (2006), in which no vertical velocity is produced by the translation of a rake instead of a grid. In this situation, the vorticity skewness should reach even larger values, emphasizing the importance of the initial conditions in the nature of the decaying rotating turbulence.

We gratefully acknowledge H. Didelle, S. Viboud and A. Aubertin for experimental help, and C. Cambon, A. Davaille, F. Doumenc, S. Galtier for fruitful discussions. This work was supported by the ANR grant no. 06-BLAN-0363-01 'HiSpeedPIV'.

Supplementary movies are available at journals.cambridge.org/flm.

REFERENCES

Bartello, P., Métais, O. & Lesieur, M. 1994 Coherent structures in rotating three-dimensional turbulence. *J. Fluid Mech.* **273**, 1–29.

Bewley, G. P, Lathrop, D. P., Maas, L. R. M & Sreenivasan, K. R. 2007 Inertial waves in rotating grid turbulence. *Phys. Fluids* **17**, 071701.

van Bokhoven, L. J. A., Cambon, C., Liechtenstein, L., Godeferd, F. S. & Clercx, H. J. H. 2008 Refined vorticity statistics of decaying rotating three-dimensional turbulence. *J. Turbul.* **9** (6), 1–24.

Bourouiba, L. & Bartello, P. 2007 The intermediate Rossby number range and two-dimensional–three-dimensional transfers in rotating decaying homogeneous turbulence. *J. Fluid Mech.* **587**, 139–161.

Cambon, C. 2001 Turbulence and vortex structures in rotating and stratified flows. *Eur. J. Mech.* B/*Fluids* **20**, 489–510.

Cambon, C. & Jacquin L. 1989 Spectral approach to non-isotropic turbulence subjected to rotation. *J. Fluid Mech.* **202**, 295–317.

Cambon, C., Mansour, N. N. & Godeferd, F. S. 1997 Energy transfer in rotating turbulence. *J. Fluid Mech.* **337**, 303–332.

Cambon, C. & Scott, J. F. 1999 Linear and nonlinear models of anisotropic turbulence. *Annu. Rev. Fluid Mech.* **31**, 1–53.

Carnevale, G. F., McWilliams, J. C., Pomeau, Y., Weiss, J. B. & Young, W. R. 1991 Evolution of vortex statistics in two-dimensional turbulence. *Phys. Rev. Lett.* **66** (21), 2735–2738.

Comte-Bellot, G. & Corrsin, S. 1966 The use of a contraction to improve the isotropy of grid-generated turbulence. *J. Fluid Mech.* **65**, 657–682.

Dalziel, S. B. 1992 Decay of rotating turbulence: some particle tracking experiments. *Appl. Sci. Res.* **49**, 217–244.

Davidson, P. A., Staplehurst, P. J. & Dalziel, S. B. 2006 On the evolution of eddies in a rapidly rotating system. *J. Fluid Mech.* **557**, 135–144.

Gence, J. N. & Frick, C. 2001 Naissance des corrélations triples de vorticité dans une turbulence statistiquement homogène soumise à une rotation. *C. R. Acad. Sci. Paris* IIb **329**, 351–356.

Godeferd, F. S. & Lollini, L. 1999 Direct numerical simulation of turbulence with confinement and rotation. *J. Fluid Mech.* **393**, 257–308.

Greenspan, H. 1968 *The Theory of Rotating Fluids*. Cambridge University Press.

Hopfinger, E. J., Browand, F. K. & Gagne, Y. 1982 Turbulence and waves in a rotating tank. *J. Fluid Mech.* **125**, 505–534.

Ibbetson, A. & Tritton, D. 1975 Experiments on turbulence in a rotating fluid. *J. Fluid Mech.* **68**, 639–672.

Jacquin, L., Leuchter, O., Cambon, C. & Mathieu, J. 1990 Homogeneous turbulence in the presence of rotation. *J. Fluid Mech.* **220**, 1–52.

Jimenez, J. 1994 Resolution requirements for velocity gradients in turbulence. *Annu. Res. Briefs.* Center for Turbulence Research, Stanford University, pp. 357–364.

Khaledi, H. A., Barri, M. & Andersson, H. I. 2009 On the stabilizing effect of the Coriolis force on the turbulent wake of a normal flat plate. *Phys. Fluids* **21**, 095104.

Kloosterziel, C. & van Heijst, J. F. 1991 An experimental study of unstable barotropic vortices in a rotating fluid. *J. Fluid Mech.* **223**, 1–24.

Lavoie, P., Avallone, G., De Gregorio, F., Romano, G. P. & Antonia, R. A. 2007 Spatial resolution of PIV for the measurement of turbulence. *Exp. Fluids* **43**, 39–51.

Longhetto, A., Montabone, L. Provenzale, A. & Didelle, H. & Giraud, C. 2002 Coherent vortices in rotating flows: a laboratory view. *Il Nuovo Cimento* **25**, 233–249.

Maas, L. R. M. 2003 On the amphidromic structure of inertial waves in a rectangular parallelepiped. *Fluid Dyn. Res.* **33**, 373–401.

McWilliams, J. C. 1984 The emergence of isolated coherent vortices in turbulent flow. *J. Fluid Mech.* **146**, 21–43.

McWilliams, J. C. 1990 The vortices of two-dimensional turbulence. *J. Fluid Mech.* **219**, 361–385.

Mohamed, M. S. & LaRue, J. 1990 The decay power law in grid-generated turbulence. *J. Fluid Mech.* **219**, 195–214.

Moisy, F., Rabaud, M. & Salsac, K. 2009 A Synthetic Schlieren method for the measurement of the topography of a liquid interface. *Exp. Fluids* **46** (6), 1021–1036.

Morinishi, Y., Nakabayashi, K. & Ren, S. Q. 2001 Dynamics of anisotropy on decaying homogeneous turbulence subjected to system rotation. *Phys. Fluids* **13** (10), 2912–2922.

Morize, C. & Moisy, F. 2006 On the energy decay of rotating turbulence in confined geometry. *Phys. Fluids* **18**, 065107.

Morize, C., Moisy, F. & Rabaud, M. 2005 Decaying grid-generated turbulence in a rotating tank. *Phys. Fluids* **17** (9), 095105.

Morize, C., Moisy, F., Rabaud M. & Sommeria, J. 2006 On the cyclone–anticyclone asymmetry in decaying rotating turbulence. In *Conference on Turbulence and Interactions TI2006, May 29–June 2, 2006*, Porquerolles, France.

Phillips, O. M. 1963 Energy transfer in rotating fluids by reflection of inertial waves. *Phys. Fluids* **6** (4), 513–520.

Poulin, F. J., Flierl, G. R. & Pedlosky, J. 2003 Parametric instability in oscillatory shear flows. *J. Fluid Mech.* **481**, 329–353.

Praud, O., Fincham, A. & Sommeria, J. 2005 Decaying grid turbulence in a strongly stratified fluid. *J. Fluid Mech.* **522**, 1–33.

Praud, O., Sommeria, J. & Fincham, A. 2006 Decaying grid turbulence in a rotating stratified fluid. *J. Fluid Mech.* **547**, 389–412.

Raffel, M., Willert, C., Wereley, S., & Kompenhans, J. 2007 *Particle Image Velocimetry*. Springer.

Saffman, P. G. 1967 Note on decay of homogeneous turbulence. *Phys. Fluids* **10**, 1349.

Smith, L. M. & Lee, Y. 2005 On near resonances and symmetry breaking in forced rotating flows at moderate Rossby number. *J. Fluid Mech.* **535**, 111–142.

Smith, L. M. & Waleffe, F. 1999 Transfer of energy to two-dimensional large scales in forced, rotating three-dimensional turbulence. *Phys. Fluids* **11** (6), 1608–1622.

Squires, K. D., Chasnov, J. R., Mansour, N. N. & Cambon, C. 1994 The asymptotic state of rotating homogeneous turbulence at high Reynolds number. In *74th Fluid Dynamics Symposium on Application of Direct and Large Eddy Simulation to Transition and Turbulence*, Chania, Greece.

Sreenivasan, K. R. & Antonia, R. A. 1997 The phenomenology of small-scale turbulence. *Annu. Rev. Fluid Mech.* **29**, 435–472.

Sreenivasan, B. & Davidson, P. A. 2008 On the formation of cyclones and anticyclones in a rotating fluid. *Phys. Fluids* **20**, 085104.

Staplehurst, P. J., Davidson, P. A. & Dalziel, S. B. 2008 Structure formation in homogeneous freely decaying rotating turbulence. *J. Fluid Mech.* **598**, 81–105.

Tavoularis, S. & Karnik, U. 1989 Further experiments on the evolution of turbulent stresses and scales in uniformly sheared turbulence. *J. Fluid Mech.* **204**, 457–478.

Waleffe, F. 1993 Inertial transfers in the helical decomposition. *Phys. Fluids* A **5** (3), 677–685.

Yoshimatsu, Y., Midorikawa, M. & Kaneda, Y. 2010 Columnar eddy formation in freely-decaying homogeneous rotating turbulence. *J. Fluid Mech.* (submitted).